CHANDRA HETGS MULTIPHASE SPECTROSCOPY OF THE YOUNG MAGNETIC O STAR θ^1 ORIONIS C

MARC GAGNÉ,[1] MARY E. OKSALA,[1,2] DAVID H. COHEN,[3] STEPHANIE K. TONNESEN,[3,4] ASIF UD-DOULA,[5]
STANLEY P. OWOCKI,[6] RICHARD H. D. TOWNSEND,[6] AND JOSEPH J. MACFARLANE[7]

ABSTRACT

We report on four *Chandra* grating observations of the oblique magnetic rotator θ^1 Ori C (O5.5 V), covering a wide range of viewing angles with respect to the star's 1060 G dipole magnetic field. We employ line-width and centroid analyses to study the dynamics of the X-ray–emitting plasma in the circumstellar environment, as well as line-ratio diagnostics to constrain the spatial location, and global spectral modeling to constrain the temperature distribution and abundances of the very hot plasma. We investigate these diagnostics as a function of viewing angle and analyze them in conjunction with new MHD simulations of the magnetically channeled wind shock mechanism on θ^1 Ori C. This model fits all the data surprisingly well, predicting the temperature, luminosity, and occultation of the X-ray–emitting plasma with rotation phase.

Subject headings: stars: early-type — stars: individual (HD 37022) — stars: magnetic fields — stars: mass loss —
stars: rotation — stars: winds, outflows — X-rays: stars

Online material: color figure

1. INTRODUCTION

θ^1 Ori C, the brightest star in the Trapezium and the primary source of ionization of the Orion Nebula, is the only O star with a measured magnetic field (Donati et al. 2002). This hot star is an unusually strong and hard X-ray source (Yamauchi & Koyama 1993; Yamauchi et al. 1996; Schulz et al. 2000), with its X-ray flux modulated on the star's 15 day rotation period (Gagné et al. 1997). Hard, time-variable X-ray emission is not expected from O stars because they do not possess an outer convective envelope to drive a solar-type magnetic dynamo.

Rather, the detection of a variable longitudinal magnetic field by Donati et al. (2002) confirms the basic picture of an oblique magnetic rotator with a dipolar surface field strength, $B \approx 1060$ G. As such, θ^1 Ori C, with its relatively strong ($\dot{M} \approx 4 \times 10^{-7}$) $M_\odot$ yr^{-1} radiation-driven wind, may be the prototype of a new class of stellar X-ray source: a young, hot star in which a hybrid magnetic wind mechanism generates strong and hard, modulated X-ray emission.

Building on the work of Shore & Brown (1990) for Ap/Bp stars, Babel & Montmerle (1997a, 1997b) first quantitatively described the mechanism whereby a radiation-driven wind in the presence of a strong, large-scale dipole magnetic field can be channeled along the magnetic field lines. In this magnetically channeled wind shock (MCWS) model,[8] flows from the two

hemispheres meet at the magnetic equator, potentially at high velocity. This head-on collision between fast wind streams can lead to very high ($T \gg 10^7$ K) shock temperatures, much higher than those seen in observations of normal O stars (e.g., ζ Pup; Hillier et al. (1993). X-ray production in O-type supergiants is attributed to the line-force instability wind shock model (Owocki et al. 1988; Feldmeier et al. 1997b), in which shocks form from interactions between wind streams that are flowing radially away from the star at moderately different speeds.

What makes the MCWS shocks more efficient than instability-driven wind shocks is the velocity contrast experienced in the shocks. The magnetically channeled wind streams collide with the cool, dense, nearly stationary, postshock plasma at the magnetic equator. The rapid deceleration of the wind plasma, and the consequent conversion of kinetic energy into heat, causes the strong, hard shocks seen in the MCWS model. This leads to high levels of X-ray emission, since a large fraction of the wind kinetic energy is converted into shock heating. In the absence of a strong magnetic field, O-star winds do not produce a fast wind running into stationary plasma; the shocks correspondingly lead to lower shock temperatures and lower luminosity.

This picture of a magnetosphere filled with plasma and co-rotating with the star is similar to the picture that has been applied to magnetic Ap/Bp stars (Shore & Brown 1990; Shore et al. 1990; Smith & Groote 2001). Indeed, Babel & Montmerle's first paper on the subject was an application to the Ap star IQ Aur (Babel & Montmerle 1997a). However, a major difference between the model's application to Ap/Bp stars and to young O stars is that the winds of O stars are significantly stronger, representing a nonnegligible fraction of the star's energy and momentum output. This hybrid magnetic wind model thus is more than a means of explaining the geometry of circumstellar material; it can also potentially explain the intense hard X-ray emission from young, magnetized hot stars (3 orders of magnitude greater for θ^1 Ori C than for IQ Aur). As has been pointed out in the context of the magnetic Ap/Bp stars, if the dipole field is tilted with respect to the rotation axis, then the rotational modulation of our viewing angle of the magnetic pole and its effect on observed flux levels and line profiles provides a important diagnostic tool. We exploit this fact by making

[1] Department of Geology and Astronomy, West Chester University, West Chester, PA 19383; mgagne@wcupa.edu.

[2] Department of Physics and Astronomy, University of Delaware, 223 Sharp Laboratory, Newark, DE 19716; meo@udel.edu.

[3] Department of Physics and Astronomy, Swarthmore College, 500 College Avenue, Swarthmore, PA 19081; dcohen1@swarthmore.edu.

[4] Department of Astronomy, Columbia University, 1328 Pupin Physics Laboratories, New York, NY 10027; stonnes@astro.columbia.edu.

[5] Department of Physics, North Carolina State University, 2700 Stinson Drive, Raleigh, NC 27695; auddoul@unity.ncsu.edu.

[6] Bartol Research Institute, University of Delaware, 217 Sharp Laboratory, Newark, DE 19716; owocki@bartol.udel.edu, rhdt@bartol.udel.edu.

[7] Prism Computational Sciences, 455 Science Drive, Madison, WI 53711; jjm@prism-cs.com.

[8] Originally referred to as the "magnetically confined wind shock model" by Babel & Montmerle (1997a), we prefer "magnetically channeled wind shock model" to emphasize the lack of complete magnetic confinement of the postshock wind plasma (ud-Doula & Owocki 2002).

several *Chandra* observations of θ^1 Ori C at different rotational phases, in order to study the dynamics and geometry of the hot, X-ray–emitting plasma in the circumstellar environment of this young, magnetized O star and thus to assess the mechanism responsible for generating the unusual levels of X-ray emission in θ^1 Ori C.

The time-independent nature of the original Babel & Montmerle model leads to a steady state configuration in which a postshock "cooling disk" forms at the magnetic equator. In their model, this disk is essentially an infinite mass sink. This has an effect on the assumed X-ray absorption properties of the disk, and it also affects the steady-state spatial, temperature, and velocity distribution of the hot, X-ray–emitting plasma, thus affecting the quantitative predictions of observables in unphysical ways. Babel & Montmerle (1997b) further assume a rigid magnetic geometry within the magnetosphere, thereby imposing a prespecified trajectory to the wind streams; namely, they are forced to flow everywhere along the local dipole field direction. In reality, if the wind kinetic energy is large enough, the magnetic field should be distorted. In the extreme case of a field that is (locally) weak compared to the wind kinetic energy, the initially closed field lines will get ripped open and the flow (and field lines) will be radial, and the focusing of the wind flow toward the equator and the associated shock heating will be minimized. Babel & Montmerle (1997b) recognized these limitations and speculated about the effects of relaxing the strong-field and steady state assumptions (see also Donati et al. 2002).

To explore these effects, ud-Doula & Owocki (2002) performed magnetohydrodynamic (MHD) simulations of radiation-driven winds in the presence of a magnetic field. Their results confirmed the basic paradigm of the Babel & Montemerle model, wherein a magnetic field channels the wind material toward the magnetic equator, where it shocks and cools. If the field is strong enough it can even confine the wind. The overall degree of such a confinement can be determined by a single dimensionless parameter, $\eta_\star$, which represents the ratio of the magnetic energy density to the wind kinetic energy density,

$$\eta_\star = \frac{B_{\mathrm{eq}}^2 R_\star^2}{\dot{M} v_\infty}, \qquad (1)$$

where B_{eq} is the equatorial dipole magnetic intensity at the stellar surface, $R_\star$ is the stellar radius, $\dot{M}$ is the mass-loss rate, and v_∞ is the terminal wind speed. For $\eta_\star \lesssim 1$, the field is relatively weak and the wind dominates over the magnetic field by ripping the field lines into a nearly radial configuration. Nonetheless, the field still manages to divert some material toward the magnetic equator, leading to a noticeable density enhancement. Because the magnetic field energy density falls off significantly faster than the wind kinetic energy density, at large radii the wind always dominates over the field, even for $\eta_\star \gg 1$. The MHD simulations reveal some phenomena not predicted by the static Babel & Montmerle model. Above the closed magnetosphere near the magnetic equator, where the field lines start to open up, the magnetically channeled wind still has a large latitudinal velocity component, leading to strong shocks.

The simulations show shock-heated wind plasma above and below the magnetic equatorial plane, where it cools and then falls along closed magnetic field lines. This cool, dense, post-shock plasma forms an unstable disk. Mass in the disk builds up until it can no longer be supported by magnetic tension, at which time it falls back down onto the photosphere. The star's

rotation and the obliquity of the magnetic axis to the rotation axis lead to periodic occultation of some of the X-ray–emitting plasma. All of these phenomena should lead to observable, viewing-angle-dependent diagnostics: temperature distribution, Doppler line broadening, line shifts, and absorption.

The initial two-dimensional MHD simulations performed by ud-Doula & Owocki (2002) were isothermal, and the shock strength and associated heating were estimated on the basis of the shock-jump velocities seen in the MHD output. For the analysis of the *Chandra* HETGS spectra discussed in this paper, however, new simulations were performed that include adiabatic cooling and radiative cooling, as well as shock heating, in the MHD code's energy equation. In this way, we make detailed, quantitative predictions of plasma temperature and hence X-ray emission for comparison with the data. Furthermore, the changes in gas pressure associated with the inclusion of heating and cooling has the potential to affect the dynamics and thus the shock physics and geometry of the magnetosphere. We thus present the most physically realistic modeling to date of X-ray production in the context of the MCWS model.

In this paper we present two new observations of θ^1 Ori C taken with the HETGS on board *Chandra*, which we analyze in conjunction with two GTO observations previously published by Schulz et al. (2000, 2003). These four observations provide good coverage of the rotational phase and hence sample a broad range of viewing angles with respect to the magnetosphere. We apply several spectral diagnostics, including line-width analysis for plasma dynamics, line-ratio analysis for distance from the photosphere, differential emission measure for the plasma temperature distribution, and overall X-ray spectral variability for the degree of occultation and absorption, to these four data sets. In this way, we characterize the plasma properties and their variation with phase, or viewing angle, allowing us to compare these results to the output of MHD simulations and assess the applicability of the MCWS model to this star.

In § 2 we describe the data and our reduction and analysis procedure. In § 3 we discuss the properties of θ^1 Ori C. In §4 we describe the MHD modeling and associated diagnostic synthesis. In § 5 we report on the results of spectral diagnostics and their variation with phase. In § 6 we discuss the points of agreement and disagreement between the modeling and the data, critically assessing the spatial distribution of the shock-heated plasma and its physical properties in light of the observational constraints and the modeling. We conclude with an assessment of the applicability of hybrid magnetic wind models to θ^1 Ori C in § 7.

2. *Chandra* OBSERVATIONS AND DATA ANALYSIS

The *Chandra* X-ray Observatory observed the Trapezium with the High Energy Transmission Grating (HETG) spectrometer twice during Cycle 1 and twice during Cycle 3. The Orion Nebula Cluster was also observed repeatedly during Cycle 4 with the ACIS-I camera with no gratings. Table 1 lists each observation's sequence number, observation ID (ObsID), UT start and end date, exposure time (in kiloseconds), average phase, and average viewing angle (in degrees). The phase was calculated using a period of 15.422 days and a zero point at MJD $= 48,832.5$ (Stahl et al. 1996). Assuming a centered oblique magnetic rotator geometry (see Fig. 1), the viewing angle α between the line of sight and the magnetic pole is specified by

$$\cos \alpha = \sin \beta \cos \phi \sin i + \cos \beta \cos i, \qquad (2)$$

TABLE 1
Chandra Observations of θ^1 Ori C

Sequence Number	ObsID	Detector	Grating	Start Date (UT)	Start Time (UT)	End Date (UT)	End Time (UT)	Exposure Time (ks)	Average Phase[a]	Viewing Angle[b] (deg)
200001............	3	ACIS-S	HETG	1999 Oct 31	05:47:21	1999 Oct 31	20:26:13	52.0	0.84	40
200002............	4	ACIS-S	HETG	1999 Nov 24	05:37:54	1999 Nov 24	15:08:39	33.8	0.38	80
200175............	2567	ACIS-S	HETG	2001 Dec 28	12:25:56	2001 Dec 29	02:00:53	46.4	0.01	4
200176............	2568	ACIS-S	HETG	2002 Feb 19	20:29:42	2002 Feb 20	10:01:59	46.3	0.47	87
200214............	4395	ACIS-I	None	2003 Jan 8	20:58:19	2003 Jan 10	01:28:41	100.0	0.44	85
200214............	3744	ACIS-I	None	2003 Jan 10	16:17:39	2003 Jan 12	14:51:52	164.2	0.58	84
200214............	4373	ACIS-I	None	2003 Jan 13	07:34:44	2003 Jan 15	08:12:49	171.5	0.75	58
200214............	4374	ACIS-I	None	2003 Jan 16	00:00:38	2003 Jan 17	23:56:05	169.0	0.92	19
200214............	4396	ACIS-I	None	2003 Jan 18	14:34:49	2003 Jan 20	13:15:31	164.6	0.09	23
200193............	3498	ACIS-I	None	2003 Jan 21	06:10:28	2003 Jan 22	02:09:20	69.0	0.23	54

[a] Assuming ephemeris $P = 15.422$ days and $MJD_0 = 48832.5$ (Stahl et al. 1996).
[b] Assuming inclination $i = 45°$ and obliquity $\beta = 42°$ (Donati et al. 2002).

where $\beta = 42°$ is the obliquity (the angle between the rotational and magnetic axes), $i = 45°$ is the inclination angle, and ϕ is the rotational phase of the observation (in degrees). In Figure 1 the arrows at each viewing angle point to Earth. As the star rotates, the viewing angle varies from $\alpha \approx 3°$ (nearly pole-on) at phase $\phi = 0.0$ to $\alpha \approx 87°$ (nearly edge-on) at phase $\phi = 0.5$. The four grating observations were obtained at $\alpha \approx 4°, 40°, 80°$, and $87°$, thus spanning the full range of possible viewing angles.[9]

The *Chandra* HETG data were taken with the ACIS-S camera in TE mode. During ObsID 3 and 4, ACIS CCDs S1-S5 were

[9] An online animation available at http://www.bartol.udel.edu/t1oc illustrates our view of the magnetosphere as a function of rotational phase.

$\alpha = 4$

B

$\alpha = 40$

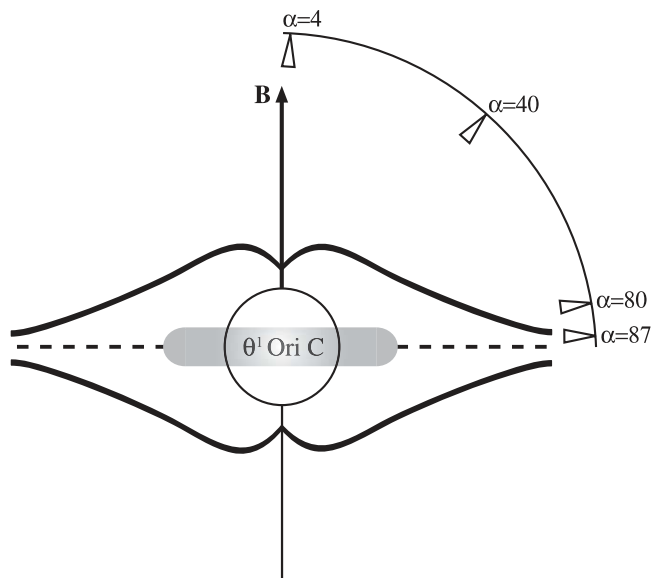θ^1 Ori C

$\alpha = 80$
$\alpha = 87$

Fig. 1.—Schematic of θ^1 Ori C and its circumstellar environment. The curved lines represent a set of magnetic field lines stretched out by the wind. The vector indicates the magnetic axis, and the dashed line represents the magnetic equatorial plane. The viewing angles in degrees with respect to the magnetic axis of the four *Chandra* observations, α, are indicated by the four labels, 4, 40, 80, and 87. The triangular arrows point to the observer. In this figure, taken from the perspective of the star's magnetic axis, the observer appears to move from $\alpha \approx 3°$ (at rotational phase 0.0) to $\alpha \approx 87°$ (at rotational phase 0.5), back to $\alpha \approx 3°$ (at rotational phase 1.0) as a result of the magnetic obliquity, $\beta = 42°$. The rotation axis, which we assume is inclined by approximately 45° to the observer, is not shown because it too would move. The hard X-ray–emitting region is shown schematically as a gray torus. At high viewing angles, the entire torus is visible (X-ray maximum). At low viewing angles, some of the torus is occulted (X-ray minimum).

used; S0 was not active. During ObsIDs 2567 and 2568, ACIS CCDs S0-S5 were used. The data were reduced using standard threads in CIAO version 2.2.1 using CALDB version 2.26. Events with standard *ASCA* grades 0, 2, 3, 4, and 6 were retained. The data for CCD S4 were destreaked because of a flaw in the serial readout that causes excess charge to be deposited along some rows. The data extraction resulted in four first-order spectra for each observation: positive and negative first-order spectra for both the medium-energy grating (MEG) and high-energy grating (HEG).

A grating auxiliary response file was calculated for each grating spectrum. The negative and positive first-order spectra were then coadded for each observation using the CIAO program ADD_GRATING_ORDERS. The four sets of MEG and HEG spectra are shown in the top four panels of Figures 2 and 3, respectively. The first-order MEG spectra from each of the four observations were then co-added to create the spectrum in the bottom panel of Figure 2. The co-added HEG spectrum is shown in the bottom panel of Figure 3. The MEG gratings have lower dispersion than the HEG gratings. However, the MEG is more efficient than the HEG above 3.5 Å. The added spectral resolution of the HEG is useful for resolving line profiles and lines that may be blended in the MEG spectrum. Because the HEG and MEG wavelength solutions were in excellent agreement, the MEG and HEG spectra were fit together to increase the signal-to-noise ratio (S/N).

The spectra show very strong line and continuum emission below 10 Å, indicating a very hot, optically thin plasma. The relatively low line-to-continuum ratio from 9 to 12 Å suggests subsolar Fe abundance. Photons with $\lambda > 24$ Å are nearly entirely absorbed by neutral hydrogen, helium, and metals in the wind of θ^1 Ori C, in the neutral lid of the Orion Nebula, and in the line-of-sight interstellar medium (ISM).

We analyzed the extracted spectra in several different ways. In § 5 we discuss the diagnostics that we bring to bear on the determination of the properties of the hot plasma, but first we describe our data analysis procedures. Our first goal was to determine centroid wavelengths, intensities, and noninstrumental line widths for the 80 or so brightest emission lines. Our second goal was to determine the basic physical properties of the X-ray–emitting plasma.

2.1. *Global Spectral Fits*

In order to determine the temperatures, emission measures, and abundances of the emitting plasma and the column density
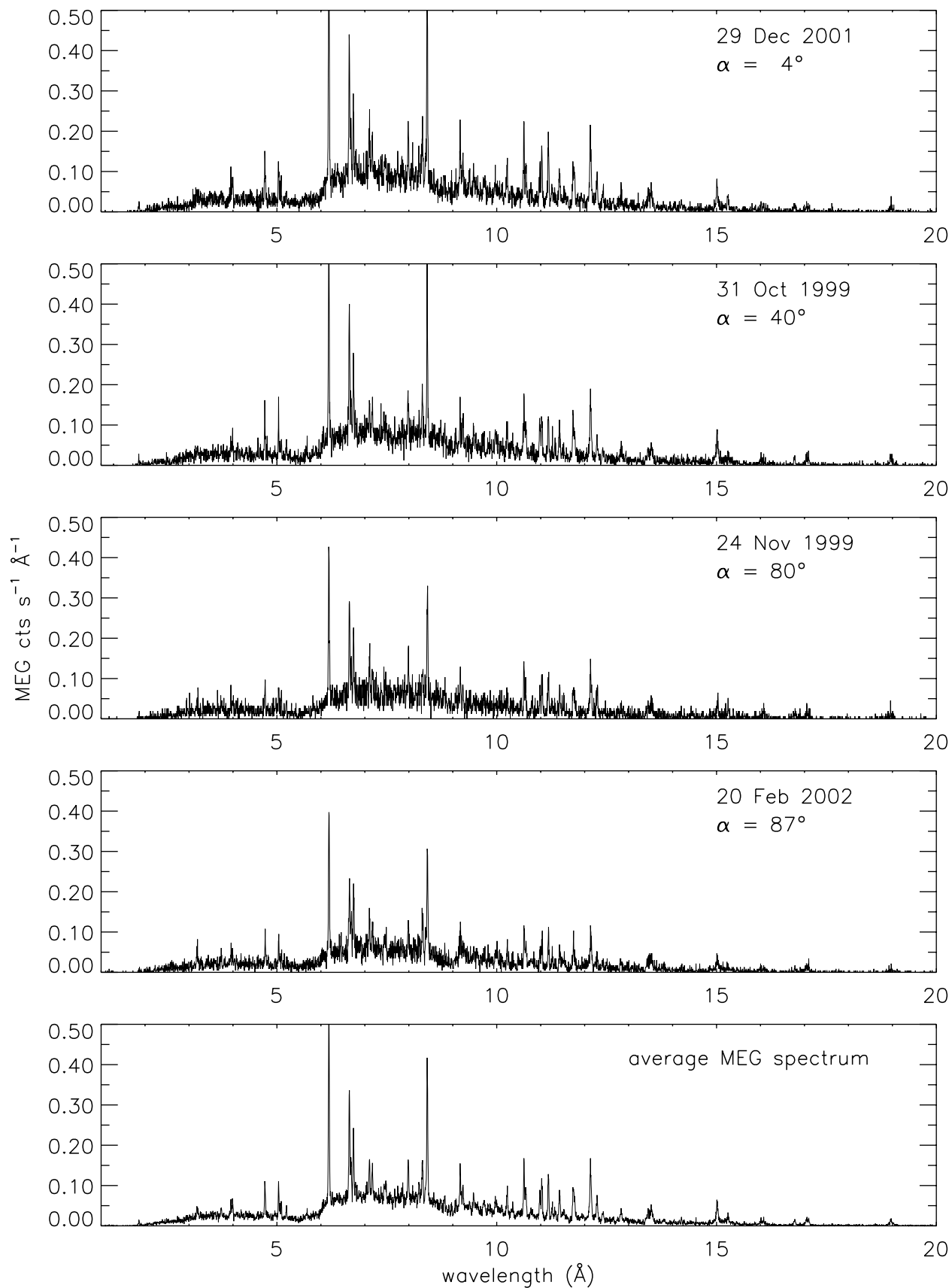
FIG. 2.—All four co-added, first-order MEG spectra, ordered according to viewing angle (pole-on to equator-on). The bottom panel shows an averaged MEG spectrum composed of the four individual spectra. The low count rate at long wavelengths is due to ISM attenuation.
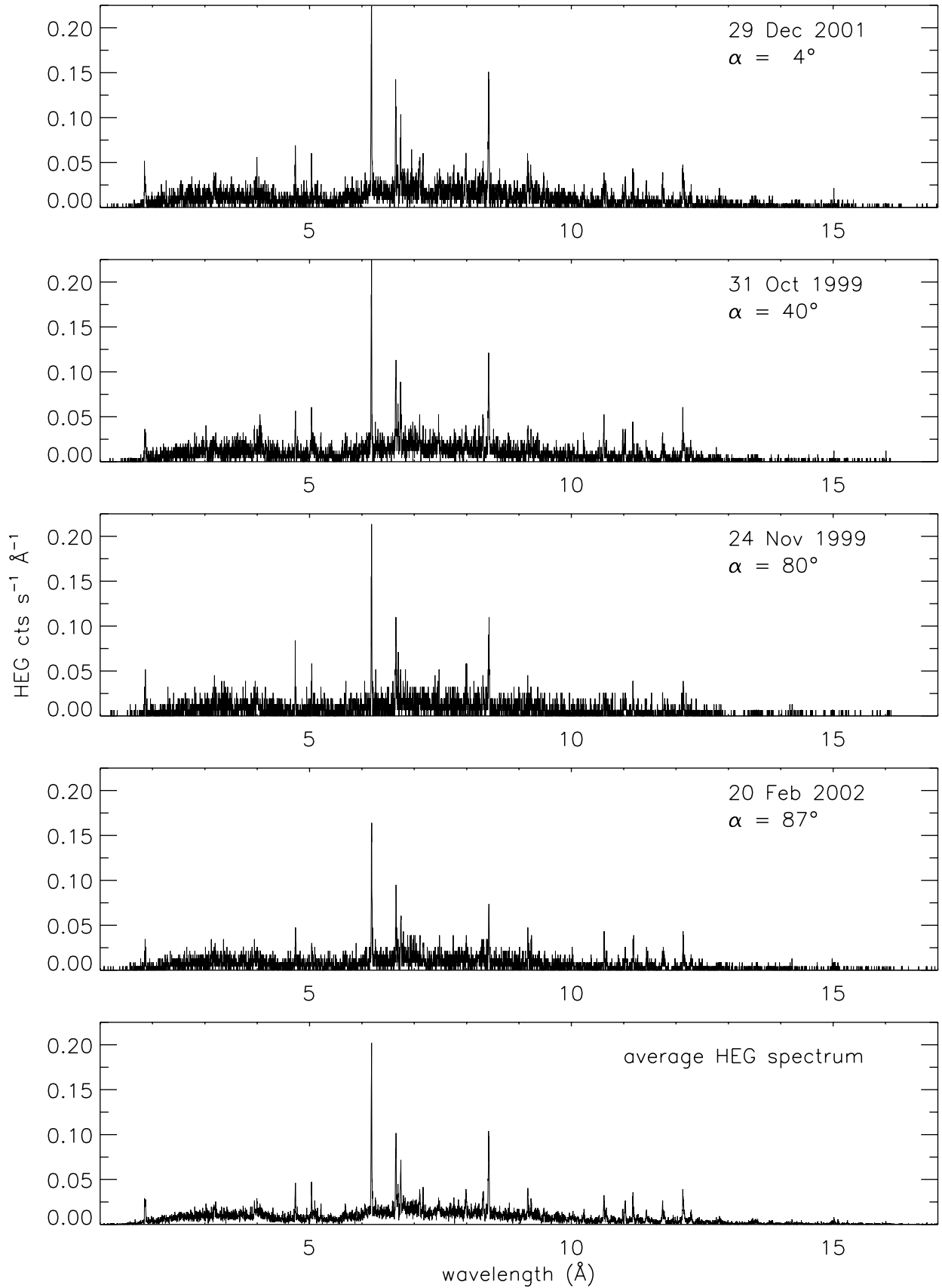
FIG. 3.—All four co-added, first-order HEG spectra, ordered according to viewing angle (pole-on to equator-on). The bottom panel shows an averaged HEG spectrum composed of the four individual spectra. The HEG has higher spectral resolution than the MEG, but lower throughput longward of approximately 3.5 Å.

of the overlying gas, we fit the HEG/MEG spectra using the ISIS[10] software package. We obtained acceptable fits to the 1.8–23 Å HEG and MEG spectra using a two-temperature variable-abundance APED[11] emission model with photoelectric absorption from neutral ISM gas (Morrison & McCammon 1983). The free parameters were the column density, the two temperatures, the two normalizations, the redshift, the turbulent velocity, and the abundances of O, Ne, Mg, Si, S, Ar, Ca, and Fe.

We note that a number of emission-measure profiles EM(T) can be used to fit the spectra, all giving rise to similar results: a dominant temperature component near 30 MK, and a second temperature peak near 8 MK. We chose the simplest model with the fewest free parameters that adequately fit the data: a two-temperature, variable abundance APEC model in ISIS. We also note that with all the thermal emission models we tried, nonsolar abundances were needed to correctly fit the emission lines.

As we discuss in § 5, we find small but significant shifts in the line centroids. The ISIS plasma emission model has one advantage over those in SHERPA and XSPEC: it explicitly and consistently accounts for thermal, nonthermal, and instrumental line broadening. The width of a line corrected for instrumental broadening is the Doppler velocity, v_D, as defined by Rybicki & Lightman (1979),

$$v_D = \frac{c}{\lambda_0} \Delta\lambda_D = \frac{c}{\lambda_0} \frac{\text{FWHM}}{\sqrt{\ln 16}} = \left(\frac{2kT}{m} + \xi^2\right)^{1/2}, \quad (3)$$

where $v_{th} = (2kT/m)^{1/2}$ is the thermal broadening component and ξ is the rms of the turbulent velocities; ξ is used simply as a standard means of parameterizing the component of the line width caused by nonthermal bulk motion (assumed to be Gaussian). As we discuss further in § 5, the nonthermal, noninstrumental width parametrized by ξ is probably the result of bulk motion of shock-heated wind plasma, and not, strictly speaking, physical microturbulence as described by Rybicki & Lightman (1979). Note that v_D and ξ thus defined are related to v_{HWHM}, often used as a velocity-width parameter when broadening is due to a stellar wind, as $v_{HWHM} = 0.83 v_D$.

The spectral analysis showed no obvious changes in abundance with phase. The best-fit abundances and 1 σ uncertainties are shown in the "Global Fit" column of Table 5. These abundances were then fixed for the fits at each rotational phase. Those best-fit parameters and 1 σ uncertainties are shown in Table 6. The most notable result of the global fitting is that most of the plasma is at $T \approx 30$ MK and that the temperatures do not vary significantly with phase. The phase-to-phase spectral variations seen in Figures 2 and 3 appear to be caused by changes in visible emission measure. One disadvantage of this type of global fitting is that the thermal emission models currently in ISIS, SHERPA, and XSPEC do not account for the effects of high density and/or UV radiation. For this, we model the individual line complexes (see § 5.2).

2.2. Line Profile Analysis

SHERPA, the CIAO spectral fitting program, was used to fit the 24 strongest line complexes of O, Ne, Mg, Si, S, Ar, Ca, and Fe in the 1.75–23 Å range. In the 3–13 Å region, the HEG and MEG spectra were simultaneously fit for each complex. Below

3 Å, the MEG spectra have low S/N and only the HEG spectra were used. Above 13 Å, the HEG spectra have low S/N and only the MEG spectra were used. Because each line complex typically contains 1–8 relatively bright lines, multiple Gaussian components were used to model the brightest lines in a complex (as estimated by their relative intensities at 30 MK in APED). Emission from continua and very faint lines across each complex was modeled simply as an additive constant. We note, e.g., that unresolved doublets were modeled as two Gaussians, with the emissivity of the fainter of the pair tied to the emissivity of the brighter. To further minimize the number of free parameters, the centroid wavelengths and widths of all lines in a complex were tied to that of the brightest line in that complex.

For example, a typical He-like line complex such as Si XIII (see Fig. 12c) was modeled with six Gaussians: the Si XIII resonant (singlet), intercombination (doublet), and forbidden (singlet) lines plus the Mg XII resonant doublet. This particular complex had six free parameters: one constant, one line width, one line shift (relative to APED), and three intensities (Si XIII resonance, one Si XIII intercombination, and Si XIII forbidden). In this case, the Mg XII emission was blended with the Si XIII forbidden line. In these cases, blending leads to higher uncertainties in the line parameters. In this example, the Mg XII line was accounted for by tying its flux to the flux of the Si XIII resonance line, scaled by the emissivity ratio of those lines in APED and the Mg/Si ratio from globally fitting the HEG/MEG spectra.

The resulting SHERPA fits are shown in the first nine columns of Table 2. The ion, transition, and rest wavelength λ_0 are from APED. Free parameters have associated 1 σ errors; tied parameters do not. As expected, line and continuum fluxes were approximately 30% higher during ObsID 2567 (viewing angle $\alpha = 4°$) than during ObsID 2568 ($\alpha = 87°$), with intermediate fluxes during ObsIDs 3 and 4.

Because SHERPA does not explicitly account for thermal and nonthermal line broadening, the individual line complexes were fit a second time with ISIS to derive the rms turbulent velocities and abundances. The ξ and relevant abundance parameters for a given line complex were allowed to vary while the emission and absorption parameters (temperatures, normalizations, other abundances, and column density) were frozen. The resulting abundances and 1 σ uncertainties are listed in the "Line Fit" column of Table 5. The Fe abundance was determined from numerous ionization stages in six line complexes. For Fe, σ is the standard deviation of these six Fe abundance fits. The individual rms turbulent velocities ξ are listed in the last two columns of Table 2.

Summarizing the results of the spectral fitting, we conclude that some elements (especially Fe) have nonsolar abundances, most of the plasma is at a temperature around 30 MK, the lines are resolved but much narrower than the terminal wind velocity, and only the overall emission measure appears to vary significantly with phase.

We note that the zeroth-order ACIS-S point-spread function (PSF) of θ^1 Ori C is substantially broader than nearby point sources and substantially broader than the nominal ACIS PSF. We have taken the best-fit model from ISIS and made MARX simulations of the zeroth-order PSF. The simulations show that the excess broadening in the zeroth-order image is a result of pileup in the ACIS-S CCD. Pixels in the core of the PSF register multiple events occurring within a single 3.2 s readout as a single higher-energy count. In the wings of the PSF, the count rate per pixel is much lower and pileup is reduced. Hence the spatial profile is less peaked than it would be without pileup. Because the count rate per pixel in the first-order lines is much lower than in zeroth order, the lines in the dispersed spectra are

---

[10] ISIS: Interactive Spectral Interpretation System, version 1.1.3.
[11] The Astrophysical Plasma Emission Database is an atomic data collection to calculate plasma continuum + emission-line spectra. See Smith et al. (2001) and references therein.

TABLE 2

HEG and MEG Line List for θ^1 Ori C: Combined Observations

Ion	Transition	λ_0 (Å)	λ (Å)	σ_λ (Å)	$10^6 f_l$ (photons cm^{-2} s^{-1})	$10^6 \sigma_f$ (photons cm^{-2} s^{-1})	v_D (km s^{-1})	σ_v (km s^{-1})	ξ^a (km s^{-1})	σ_ξ (km s^{-1})
Fe XXV	$1s2p\ ^1P_1 \rightarrow 1s^2\ ^1S_0$	1.8504	1.8498	0.0009	26.23	4.86	409	...	300	...
	$1s2p\ ^3P_2 \rightarrow 1s^2\ ^1S_0$	1.8554	1.8548	...	10.00	2.62	409	...	300	...
	$1s2p\ ^3P_1 \rightarrow 1s^2\ ^1S_0$	1.8595	1.8589	...	9.57	...	409	...	300	...
	$1s2s\ ^3S_1 \rightarrow 1s^2\ ^1S_0$	1.8682	1.8676	...	28.47	4.56	409	...	300	...
Ca XIX	$1s2p\ ^1P_1 \rightarrow 1s^2\ ^1S_0$	3.1772	3.1746	0.0013	8.70	1.62	426	263	300	...
	$1s2p\ ^3P_2 \rightarrow 1s^2\ ^1S_0$	3.1891	3.1865	...	4.32	0.88	426	...	300	...
	$1s2p\ ^3P_1 \rightarrow 1s^2\ ^1S_0$	3.1927	3.1901	...	3.66	...	426	...	300	...
	$1s2s\ ^3S_1 \rightarrow 1s^2\ ^1S_0$	3.2110	3.2083	...	6.93	1.52	426	...	300	...
Ar XVIII	$2p\ ^2P_{3/2} \rightarrow 1s\ ^2S_{1/2}$	3.7311	3.7308	0.0016	6.48	1.16	400	...	400	...
	$2p\ ^2P_{1/2} \rightarrow 1s\ ^2S_{1/2}$	3.7365	3.7362	...	3.10	...	400	...	400	...
	$1s2p\ ^1P_1 \rightarrow 1s^2\ ^1S_0$	3.9491	3.9489	0.0009	13.02	1.91	413	132	300	...
Ar XVII	$1s2p\ ^3P_2 \rightarrow 1s^2\ ^1S_0$	3.9659	3.9657	...	3.38	0.75	413	...	300	...
	$1s2p\ ^3P_1 \rightarrow 1s^2\ ^1S_0$	3.9694	3.9692	...	3.46	...	413	...	300	...
S XVI	$3p\ ^2P_{3/2} \rightarrow 1s\ ^2S_{1/2}$	3.9908	3.9906	...	2.44	...	413	...	300	...
Ar XVII	$3p\ ^2P_{1/2} \rightarrow 1s\ ^2S_{1/2}$	3.9920	3.9918	...	1.22	...	413	...	300	...
	$1s2s\ ^3S_1 \rightarrow 1s^2\ ^1S_0$	3.9942	3.9940	...	12.37	1.95	413	...	300	...
S XVI	$2p\ ^2P_{3/2} \rightarrow 1s\ ^2S_{1/2}$	4.7274	4.7270	0.0006	41.28	2.21	539	77	478	82
	$2p\ ^2P_{1/2} \rightarrow 1s\ ^2S_{1/2}$	4.7328	4.7324	...	19.73	...	539	...	478	...
S XV	$1s2p\ ^1P_1 \rightarrow 1s^2\ ^1S_0$	5.0387	5.0382	0.0005	50.53	3.15	331	55	b	...
	$1s2p\ ^3P_2 \rightarrow 1s^2\ ^1S_0$	5.0631	5.0626	...	6.54	0.98	331	...	...	...
	$1s2p\ ^3P_1 \rightarrow 1s^2\ ^1S_0$	5.0665	5.0660	...	9.39	...	331	...	...	...
	$1s2s\ ^3S_1 \rightarrow 1s^2\ ^1S_0$	5.1015	5.1010	...	21.92	2.51	331	...	...	...
Si XIV	$2p\ ^2P_{3/2} \rightarrow 1s\ ^2S_{1/2}$	6.1804	6.1803	0.0002	75.47	1.60	355	23	305	28
	$2p\ ^2P_{1/2} \rightarrow 1s\ ^2S_{1/2}$	6.1858	6.1857	...	36.15	...	355	...	305	...
Si XIII	$1s2p\ ^1P_1 \rightarrow 1s^2\ ^1S_0$	6.6479	6.6480	0.0003	61.40	1.88	370	21	b	...
	$1s2p\ ^3P_2 \rightarrow 1s^2\ ^1S_0$	6.6850	6.6851	...	14.04	1.03	370	...	...	...
	$1s2p\ ^3P_1 \rightarrow 1s^2\ ^1S_0$	6.6882	6.6883	...	5.40	...	370	...	...	...
Mg XII	$4p\ ^2P_{3/2} \rightarrow 1s\ ^2S_{1/2}$	6.7378	6.7379	...	7.86	...	370	...	...	...
	$4p\ ^2P_{1/2} \rightarrow 1s\ ^2S_{1/2}$	6.7382	6.7383	...	3.93	...	370	...	...	...
Si XIII	$1s2s\ ^3S_1 \rightarrow 1s^2\ ^1S_0$	6.7403	6.7404	...	18.98	1.45	370	...	...	...
Mg XII	$3p\ ^2P_{3/2} \rightarrow 1s\ ^2S_{1/2}$	7.1058	7.1039	0.0009	10.97	0.77	360	54	311	54
	$3p\ ^2P_{1/2} \rightarrow 1s\ ^2S_{1/2}$	7.1069	7.1050	...	5.25	...	360	...	311	...
Fe XXIV	$1s^25p\ ^2P_{3/2} \rightarrow 1s^22s\ ^2S_{1/2}$	7.1690	7.1687	0.0010	8.49	0.74	360	...	311	...
	$1s^25p\ ^2P_{1/2} \rightarrow 1s^22s\ ^2S_{1/2}$	7.1690	7.1687	...	4.15	...	360	...	311	...
	$1s^24p\ ^2P_{3/2} \rightarrow 1s^22s\ ^2S_{1/2}$	7.9857	7.9837	0.0009	13.36	0.81	363	63	336	61
	$1s^24p\ ^2P_{1/2} \rightarrow 1s^22s\ ^2S_{1/2}$	7.9960	7.9940	...	6.81	...	363	...	336	...
Mg XII	$2p\ ^2P_{3/2} \rightarrow 1s\ ^2S_{1/2}$	8.4192	8.4183	0.0003	47.73	1.25	364	20	328	21
	$2p\ ^2P_{1/2} \rightarrow 1s\ ^2S_{1/2}$	8.4246	8.4237	...	22.91	...	364	...	328	...
Mg XI	$1s2p\ ^1P_1 \rightarrow 1s^2\ ^1S_0$	9.1687	9.1693	0.0007	28.89	1.68	415	49	b	...
	$1s2p\ ^3P_2 \rightarrow 1s^2\ ^1S_0$	9.2282	9.2288	...	2.17	0.19	415	...	...	...
	$1s2p\ ^3P_1 \rightarrow 1s^2\ ^1S_0$	9.2312	9.2318	...	15.20	...	415	...	...	...
	$1s2s\ ^3S_1 \rightarrow 1s^2\ ^1S_0$	9.3143	9.3149	...	1.36	1.15	415	...	...	...
Fe XXIV	$1s^23p\ ^2P_{3/2} \rightarrow 1s^22s\ ^2S_{1/2}$	10.6190	10.6205	0.0006	44.26	1.77	316	26	288	30
	$1s^23p\ ^2P_{1/2} \rightarrow 1s^22s\ ^2S_{1/2}$	10.6630	10.6645	...	23.28	...	316	...	288	...
Fe XXIII	$1s^22s3p\ ^1P_1 \rightarrow 1s^22s^2\ ^1S_0$	10.9810	10.9821	...	25.83	1.90	300	...	263	...
	$1s^22s3p\ ^3P_1 \rightarrow 1s^22s^2\ ^1S_0$	11.0190	11.0201	...	11.39	...	300	...	263	...

TABLE 2—*Continued*

Ion	Transition	λ_0 (Å)	λ (Å)	σ_λ (Å)	$10^6 f_l$ (photons cm^{-2} s^{-1})	$10^6 \sigma_f$ (photons cm^{-2} s^{-1})	v_D (km s^{-1})	σ_v (km s^{-1})	ξ^a (km s^{-1})	σ_ξ (km s^{-1})
Fe xxiv	$1s^2 3d\ ^2D_{3/2} \rightarrow 1s^2 2p\ ^2P_{1/2}$	11.0290	11.0301	0.0007	30.29	1.61	300	27	263	31
	$1s^2 3d\ ^2D_{5/2} \rightarrow 1s^2 2p\ ^2P_{3/2}$	11.1760	11.1744	0.0006	42.87	2.13	236	33	213	38
	$1s^2 3d\ ^2D_{3/2} \rightarrow 1s^2 2p\ ^2P_{3/2}$	11.1870	11.1854	...	4.67	...	236	...	213	...
Fe xxiii....................	$1s^2 2s3d\ ^1D_2 \rightarrow 1s^2 2s2p\ ^1P_1$	11.7360	11.7413	0.0006	48.87	2.78	387	37	387	40
Fe xxii	$1s^2 2s^2 3d\ ^2D_{3/2} \rightarrow 1s^2 2s^2 2p\ ^2P_{1/2}$	11.7700	11.7753	...	25.58	2.40	387	...	387	...
Ne x.........................	$2p\ ^2P_{3/2} \rightarrow 1s\ ^2S_{1/2}$	12.1321	12.1300	0.0007	56.30	2.17	351	36	488	35
	$2p\ ^2P_{1/2} \rightarrow 1s\ ^2S_{1/2}$	12.1375	12.1354	...	27.05	...	351	...	488	...
Fe xxiii....................	$1s^2 2s3s\ ^1S_0 \rightarrow 1s^2 2s2p\ ^1P_1$	12.1610	12.1589	...	21.17	...	351	...	488	...
Ne ix......................	$1s2p\ ^1P_1 \rightarrow 1s^2\ ^1S_0$	13.4473	13.4386	0.0029	33.29	4.09	623	86	b	...
Fe xix	$2s^2 2p^3 3d\ ^3S_1 \rightarrow 2s^2 2p^4\ ^3P_2$	13.4620	13.4533	...	5.93	0.61	623	...	...	...
	$1s^2 2s^2 2p_{1/2} 2p_{3/2}^2 3d_{3/2} \rightarrow 2s^2 2p^4\ ^3P_2$	13.4970	13.4883	...	10.38	...	623	...	...	...
Fe xxi	$1s^2 2s2p_{1/2}^2 3s \rightarrow 1s^2 2s2p^3\ ^3D_1$	13.5070	13.4983	...	9.14	...	623	...	...	...
Fe xix	$2s^2 2p^3 3d\ ^3D_3 \rightarrow 2s^2 2p^4\ ^3P_2$	13.5180	13.5093	...	22.90	...	623	...	...	...
Ne ix......................	$1s2p\ ^3P_2 \rightarrow 1s^2\ ^1S_0$	13.5503	13.5416	...	0.99	...	623	...	...	...
	$1s2p\ ^3P_1 \rightarrow 1s^2\ ^1S_0$	13.5531	13.5444	...	25.38	4.10	623	...	...	...
	$1s2s\ ^3S_1 \rightarrow 1s^2\ ^1S_0$	13.6990	13.6903	...	0.41	2.77	623	...	...	...
Fe xx	$1s^2 2s^2 2p_{1/2} 2p_{3/2} 3p_{3/2} \rightarrow 2s2p^4\ ^4P_{3/2}$	14.9978	14.9993	...	0.10	0.33	614	...	700	...
Fe xix	$2s^2 2p^3 3s\ ^1D_2 \rightarrow 2s^2 2p^4\ ^1D_2$	15.0117	15.0132	...	1.42	...	614	...	700	...
Fe xvii	$2s^2 2p^5 3d\ ^1P_1 \rightarrow 2s^2 2p^6\ ^1S_0$	15.0140	15.0155	0.0019	82.64	5.75	614	67	700	78
Fe xx	$1s^2 2s^2 2p_{3/2}^2 3p_{3/2} \rightarrow 2s2p^4\ ^2D_{5/2}$	15.0164	15.0176	...	0.26	...	614	...	700	...
Fe xviii....................	$2s^2 2p^4 3s\ ^2P_{3/2} \rightarrow 2s^2 2p^5\ ^2P_{3/2}$	16.0040	16.0074	...	13.34	2.01	325	...	456	...
O viii........................	$3p\ ^2P_{3/2} \rightarrow 1s\ ^2S_{1/2}$	16.0055	16.0089	0.0032	5.78	2.57	325	93	456	67
	$3p\ ^2P_{1/2} \rightarrow 1s\ ^2S_{1/2}$	16.0067	16.0101	...	2.77	...	325	...	456	...
Fe xviii....................	$2s^2 2p^4 3s\ ^4P_{5/2} \rightarrow 2s^2 2p^5\ ^2P_{3/2}$	16.0710	16.0662	0.0042	16.41	...	325	...	456	...
Fe xix	$1s^2 2s^2 2p_{1/2} 2p_{3/2}^2 3p_{1/2} \rightarrow 2s2p^5\ ^3P_2$	16.1100	16.1134	...	8.90	...	325	...	456	...
Fe xvii	$2s^2 2p^5 3s\ ^1P_1 \rightarrow 2s^2 2p^6\ ^1S_0$	16.7800	16.7781	0.0033	34.25	4.87	431	85	456	...
Fe xix	$1s^2 2s^2 2p_{1/2} 2p_{3/2}^2 3p_{3/2} \rightarrow 2s2p^5\ ^1P_1$	17.0311	17.0299	...	1.29	...	313	...	290	...
	$1s^2 2s^2 2p_{1/2}^2 2p_{3/2} 3p_{1/2} \rightarrow 2s2p^5\ ^3P_1$	17.0396	17.0382	...	0.33	...	313	...	290	...
Fe xvii	$2s^2 2p^5 3s\ ^3P_1 \rightarrow 2s^2 2p^6\ ^1S_0$	17.0510	17.0498	0.0029	32.82	5.16	313	64	290	87
	$2s^2 2p^5 3s\ ^3P_2 \rightarrow 2s^2 2p^6\ ^1S_0$	17.0960	17.0948	...	29.00	4.97	313	...	290	...
O viii........................	$2p\ ^2P_{3/2} \rightarrow 1s\ ^2S_{1/2}$	18.9671	18.9677	0.0037	67.49	9.54	888^c	240	851	146
	$2p\ ^2P_{1/2} \rightarrow 1s\ ^2S_{1/2}$	18.9725	18.9731	...	32.53	...	888	...	851	...
O vii	$1s2p\ ^1P_1 \rightarrow 1s^2\ ^1S_0$	21.6015	21.5917	0.0113	16.98	9.19	292	...	b	...
	$1s2p\ ^3P_2 \rightarrow 1s^2\ ^1S_0$	21.8010	21.7912	...	5.82	3.80	292	...	...	...
	$1s2p\ ^3P_1 \rightarrow 1s^2\ ^1S_0$	21.8036	21.7938	...	8.60	...	292	...	...	...
	$1s2s\ ^3S_1 \rightarrow 1s^2\ ^1S_0$	22.0977	22.0879	...	0.00	6.20	292	...	...	...

NOTE.—Nonzero errors are reported for free parameters only.

[a] ξ is the microturbulant velocity as defined by, e.g., Rybicki & Lightman (1979). Note that the ISIS plasma model explicitly accounts for thermal broadening. Hence, $\xi < v_D$.

[b] He-like complexes were not fit in ISIS because the APEC model does not account for suppression of the forbidden lines as a result of far-UV photoexcitation.

[c] O viii was fit using a two-Gaussian model; a narrow component with Doppler width fixed at $v_D = 300$ km s^{-1} and a broad component with best-fit $v_D = 1153$ km s^{-1}. The v_D reported above is the flux-weighted average of the two Doppler widths.

TABLE 3
STELLAR AND WIND PARAMETERS

Property[a]	Cool Model	Hot Model
Spectral Type	O7 V	O5.5 V
$T_{\rm eff}$ (K)..	42,280	44,840
$\log L(L_{\odot})$......................................	5.4	5.4
$R(R_{\odot})$..	9.1	8.3
$\log q_0$ (photons cm^{-2} s^{-1})......................	24.4	24.6
$\log q_1$ (photons cm^{-2} s^{-1})......................	23.6	23.9
$\log q_2$ (photons cm^{-2} s^{-1})......................	17.4	18.5
$\dot{M}$ ($M_{\odot}$ yr^{-1})................................	5.5×10^{-7}	1.4×10^{-6}
v_{∞} (km s^{-1})...	2760	2980

[a] The values q_0, q_1, and q_2 are the numbers of photons per unit area per unit time from the stellar surface $R_{\star}$ shortward of 912, 504, and 228 Å, capable of ionizing H I, He I, and He II, respectively.

not broadened by pileup. We conclude that the measured line velocities are *not* caused by instrumental effects. Noninstrumental Gaussian line shapes provide adequate fits to the data. Non-Gaussian line shapes, while perhaps present, could only be detected with higher S/N data.

3. PROPERTIES OF θ^1 Ori C

In order to put the results of the spectral fitting and the MHD modeling into a physical context, we must first specify the stellar and wind parameters of θ^1 Ori C, as well as elaborate on the geometry and distribution of circumstellar matter, as constrained by previous optical and UV measurements. The spectral type of the star is usually taken to be O6 V or O7 V, although its spectral variability was first noted by Conti (1972). Donati et al. (2002) assume a somewhat hot effective temperature, $T_{\rm eff} = 45,500$ K, which is based on the O5.5 V type used by Howarth & Prinja (1989), which itself is an average of Walborn's (1981) range of O4–O7. Walborn (1981) showed that lines often used to determine spectral type (He I λ4471, He II λ4542 and λ4686) are highly variable on timescales of about a week, suggesting a period "on the order of a few weeks." He compared θ^1 Ori C's line-profile variations to those of the magnetic B2 Vp star σ Ori E, even noting then that θ^1 Ori C's X-ray emission, recently discovered with the *Einstein Observatory*, may be related to its He II λ4686 emission.

Based on a series of Hα and He II λ4686 spectra obtained over many years, Stahl et al. (1993, 1996) and Reiners et al. (2000) have determined that the inclination angle of θ^1 Ori C is $i \approx 45°$ and the rotational period $P = 15.422 \pm 0.002$ days. The inclination angle estimate is based on arguments about the symmetry of the light curve and spectral variability, as well as plausibility arguments based on the inferred stellar radius. As expected from its long rotation period, θ^1 Ori C's projected rotational velocity is quite low, with Reiners et al. (2000) finding a value of $v \sin i = 32 \pm 5$ km s^{-1} using the O III λ5592 line core.

The Zeeman signature measurements of Donati et al. (2002) indicate a strong dipole field, with no strong evidence for higher order field components. The five sets of Stokes parameters indicate a magnetic obliquity $\beta \approx 42°$ if $i = 45°$. These numbers then imply a photospheric polar magnetic field strength of $B_p = 1060 \pm 90$ G. The obliquity and polar field strength take on modestly different values if the inclination angle is assumed to be as small as $i = 25°$ or as large as $i = 65°$.

As a result of these various determinations of stellar properties, we adopt two sets of stellar parameters that likely bracket those of θ^1 Ori C. These are listed in Table 3, and are based on the PHOENIX spherical non-LTE model atmospheres of Aufdenberg (2001).

The theoretical wind values listed in Table 3 are consistent with the observed values of $\dot{M} = 4 \times 10^{-7}\, M_{\odot}$ yr^{-1} (Howarth & Prinja 1989) and $v_{\infty} \approx 2500$ km s^{-1} (Stahl et al. 1996). The stellar wind properties, as seen in UV resonance lines, are modulated on the rotation period of the star (Walborn & Nichols 1994; Reiners et al. 2000), which, when combined with variable Hα (Stahl et al. 1996) and the new measurement of the variable magnetic field (Donati et al. 2002), lead to a coherent picture of an oblique magnetic rotator, with circumstellar material channeled along the magnetic equator. This picture is summarized in Figure 1, which also indicates the viewing angle relative to the magnetic field for our four *Chandra* observations.

When we see the system in the magnetic equatorial plane, the excess UV wind absorption is greatest. When we see the system magnetic pole on, the UV excess is at its minimum, while the longitudinal magnetic field strength is maximum, as are the X-ray and Hα emission (Stahl et al. 1993; Gagné et al. 1997). These results are summarized in Figure 4, where we show
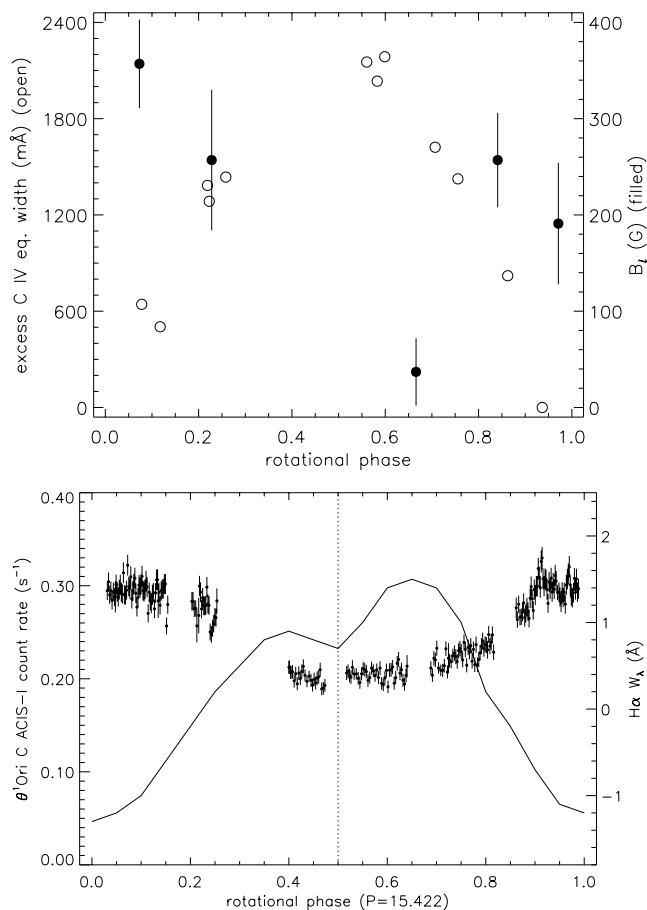

FIG. 4.—Phase-folded light curves of θ^1 Ori C. *Top:* Open circles indicate the excess C IV equivalent width (left axis) taken from Walborn & Nichols (1994) and phased to the ephemeris of Stahl et al. (1996): period $P = 15.422$ days and epoch MJD$_0$ = 48832.50. Maximum C IV absorption occurs near phase 0.5 ($\alpha = 3°$) as a result of outflowing plasma in the magnetic equatorial plane. Note that Walborn & Nichols (1994) calculate W_{λ} by subtracting the *IUE* spectrum at a given phase from the *IUE* spectrum with the shallowest line profile, then calculating the equivalent width of the line in the difference spectrum. Filled circles show the longitudinal magnetic field strength, B_l (right axis), as measured by Donati et al. (2002) using the same ephemeris. Note that Walborn & Nichols (1994) and Donati et al. (2002) used different period estimates. The B_l is maximum near phase 0.0 when the magnetic pole is in the line of sight. *Bottom:* Hα equivalent width (*solid curve*) from Stahl et al. (1996). The data points with error bars represent the ACIS-I count rate from the 850 ks *Chandra* Orion Ultra-Deep Project. X-ray and Hα maxima occur at low viewing angles when the entire X-ray torus is visible; the minima occur when part of the X-ray torus is occulted by the star.

14 days of data from the 850 ks *Chandra* Orion Ultra-Deep Project. These data were obtained with the ACIS-I camera with no gratings. Because θ^1 Ori C's count rate far exceeds the read-out rate of the ACIS-I CCD, the central pixels of the source suffer from severe pileup. For Figure 4 (*bottom*), counts were extracted from an annular region in the wings of the PSF where pileup was negligible As a result, the *Chandra* light curve does not show the absolute count rate in the ACIS-I instrument. The light curve shows long-term variability induced by rotation and occultation and statistically significant short-term variability that may reflect the dynamic nature of the magnetically chan-neled wind shocks.

These four different observational results are consistent with this picture provided that the Hα emission is produced in the postshock plasma near the magnetic equatorial plane. Smith & Fullerton (2005) have reanalyzed the 22 high-dispersion *IUE* spectra of θ^1 Ori C and reinterpreted the time-variable UV and optical line profiles in terms of the magnetic geometry of Donati et al. (2002). Smith & Fullerton (2005) find that the C IV and N V lines at phase 0.5 (nearly edge-on) are characterized by high, negative-velocity absorptions and lower, positive-velocity emis-sion, superposed on the baseline P Cygni profile. Similarly, some of the optical Balmer-line and He II emissions appear to be pro-duced by postshock gas falling back onto to the star. In the fol-lowing sections, we further constrain and elaborate on this picture by using several different X-ray diagnostics in conjunction with MHD modeling.

We note finally that θ^1 Ori C has at least one companion. Weigelt et al. (1999) find a companion at 33 mas via infrared speckle interferometry. Donati et al. (2002) estimate its orbital period to be 8–16 yr and Schertl et al. (2003) estimate its spec-tral type as B0–A0. This places the companion at 15 AU, too far to significantly interact with the wind or the magnetic field of θ^1 Ori C. The amplitude and timescale of the X-ray luminosity var-iations cannot be caused by colliding-wind emission with the companion, by occultation by the companion, or by the com-panion itself (Gagné et al. 1997).

4. MAGNETOHYDRODYNAMIC MODELING OF THE MAGNETICALLY CHANNELED WIND OF θ^1 ORI C

4.1. *Basic Formulation*

As discussed in § 1, we have carried out MHD simulations tailored specifically for the interpretation of the θ^1 Ori C X-ray data presented in this paper. Building upon the full MHD mod-els by ud-Doula & Owocki (2002), these simulations are self-consistent in the sense that the magnetic field geometry, which is initially specified as a pure dipole with a polar field strength of 1060 G, is allowed to adjust in response to the dynamical influ-ence of the outflowing wind. As detailed below, a key improve-ment over the isothermal simulations of ud-Doula & Owocki (2002) is that we now use an explicit energy equation to follow shock heating of material to X-ray–emitting temperatures.

The overall wind driving, however, still follows a local CAK/Sobolev approach that suppresses the "line deshadowing instability" for structure on scales near and below the Sobolev length, $l \approx v_{th}r/v \approx 10^{-2}r$, where r is the radius and v and v_{th} are the flow and thermal speeds, respectively (Lucy & Solomon 1970; MacGregor et al. 1979; Owocki & Rybicki 1984, 1985). For nonmagnetic winds, one-dimensional simulations using a nonlocal, non-Sobolev formulation for the line force (Owocki et al. 1988; Owocki & Puls 1999; Runacres & Owocki 2002) show that this instability can lead to embedded weak shock

structures that might reproduce the soft X-ray emission (Feldmeier 1995; Feldmeier et al. 1997b) observed in hot stars like ζ Pup (Waldron & Cassinelli 2001; Kramer et al. 2003a). However, it seems unlikely that such small-scale, weak-shock structures can explain the much harder X-rays observed from θ^1 Ori C. Given, moreover, the much greater computational expense of the nonlocal line-force computation, especially for the two-dimensional models computed here (Dessart & Owocki 2003, 2005), we retain the much simpler, CAK/Sobolev form for the line driving. In the absence of a magnetic field, such an approach just relaxes to the standard, steady-state, spherically symmetric CAK solution. As such, the extensive flow structure, and associated hard X-ray emission, obtained in the MHD models here are a direct consequence of the wind channeling by the as-sumed magnetic dipole originating from the stellar surface.

Since the ~15 day rotation period of θ^1 Ori C is much longer than the characteristic wind flow time of a fraction of a day, we expect that associated centrifugal and coriolis terms should have limited effect on either the wind dynamics or the magnetic field topology. Thus, for simplicity, and to retain the compu-tational efficiency of axisymmetry, the numerical simulations here formally assume no rotation. However, in comparing the resulting X-ray emission to observations, we do account for the rotational modulation arising from the change in observer view-ing angle with rotational phase, using the estimated inclination angle $i \approx 45°$ between the rotation axis and the observer's line of sight, and obliquity $\beta \approx 42°$.

4.2. *Energy Balance with Shock Heating and Radiative Cooling*

In order to derive quantitative predictions for the X-ray emis-sion from the strong wind shocks that arise from the magnetic confinement, the simulations here extend the isothermal models of ud-Doula & Owocki (2002) to include a detailed treatment of the wind energy balance, accounting for both shock heating and radiative cooling. Specifically, the total time derivative (D/Dt) of wind internal energy density e [related to the gas pressure p by $e = p/(\gamma - 1) = (3/2)p$ for a ratio of specific heats $\gamma = 5/3$ appropriate for a monatomic gas] is computed from

$$\rho \frac{D(e/\rho)}{Dt} = -\rho \nabla \cdot \boldsymbol{p} + H - C, \qquad (4)$$

where ρ is the mass density, and H and C represent volumetric heating and cooling terms. In steady hot-star winds, the flow is kept nearly isothermal at roughly the stellar effective temper-ature (few $\times 10^4$ K) through the near balance between heating by photoionization from the underlying star and cooling by radiative emission (mostly in lines; see, e.g., Drew 1989). In such steady outflows, both the heating and cooling terms are intrinsically much larger than the adiabatic cooling from the work expansion, as given by the first term on the right-hand side of the energy equation.

But in variable, structured winds with compressive shocks, this first term can now lead to strong compressive heating, with some material now reaching much higher, X-ray–emitting temperatures. Through numerical time integrations of the en-ergy equation, our MHD simulations account directly for this compressive heating near shocks, also imposing a floor value at the photospheric effective temperature to account for the effect of photoionization heating on the relatively cool, expanding regions. In the simulations, the temperature of the far wind is $T = 45,700$ K, slightly warmer than the O5.5 photosphere (see Table 3).

The shock-heated material is cooled by the radiative loss term, which is taken to follow the standard form for an optically thin plasma,

$$C = n_e n_H \mathcal{L}(T), \qquad (5)$$

where n_e and n_H are the numbers densities for electrons and hydrogen atoms, and T is the electron temperature.

A proper radiative cooling calculation must include many different ionic species, with all the possible lines (Raymond et al. 1976; MacDonald & Bailey 1981), the exact form of the cooling function $\mathcal{L}(T)$ depending on the composition of heavy elements. Detailed calculations for the typical case of solar abundances show that, at low temperatures, the cooling function $\mathcal{L}(T)$ increases approximately monotonically with temperature, reaching a maximum, $\mathcal{L} \approx 3 \times 10^{-22}$ ergs cm^3 s^{-1}, at $T \approx 2 \times 10^5$ K (Raymond et al. 1976), where the cooling is dominated by collisional excitation of abundant lithium-like atoms. Above $T \approx 2 \times 10^5$ K, $\mathcal{L}(T)$ decreases with temperature, except for some prominent bumps at approximately 2 and 8 MK. Above $T \approx 3 \times 10^7$ K, thermal bremsstrahlung radiation dominates and the cooling function turns over again, increasing with temperature. In our simulations, we follow the tabulated form of the MacDonald & Bailey (1981) cooling curve based on this solar-abundance recipe.

4.3. Simulations Results for Temperature and Emission Measure

One of the key results of ud-Doula & Owocki (2002) is that the overall degree to which the wind is influenced by the magnetic field depends largely on a single parameter, the magnetic confinement parameter, $\eta_\star$, defined by equation (1). For our MHD simulations of the magnetic wind confinement in θ^1 Ori C, we use $\eta_\star = 7.5$, based on an assumed stellar radius $R_\star \approx 9 R_\odot$ (see Table 3), $B_{eq} = \frac{1}{2}B_{p\approx530}$ G (Donati et al. 2002). The simulation produces an average mass-loss rate $\dot{M} \approx 4 \times 10^{-7} M_\odot$ yr^{-1} (Howarth & Prinja 1989), and terminal wind speed $v_\infty \approx 1400$ km s^{-1}. Thus, we anticipate that, at least qualitatively, the simulation results for θ^1 Ori C should be similar to the strong magnetic confinement case ($\eta_\star = 10$) shown in Figure 9 of ud-Doula & Owocki (2002), allowing, however, for differences from the inclusion here of a full energy equation instead of the previous assumption of a strictly isothermal outflow.

We note that θ^1 Ori C's observed terminal wind speed derived from *IUE* high-resolution spectra (Howarth & Prinja 1989; Prinja et al. 1990; Walborn & Nichols 1994) varies significantly, with $v_\infty \approx 510$ km s^{-1} at rotational phase 0.1, when the wind absorption is weak (see Fig. 4, *top panel*). θ^1 Ori C's wind speed and mass-loss rate are lower than those of other mid-O stars and lower than expected from model atmosphere calculations (see Table 3). In the interpretation of Smith & Fullerton (2005) and Donati et al. (2002), most of the wind is channeled to the magnetic equatorial region. Thus, $\dot{M}$ and v_∞ are low near X-ray maximum (phase 0.0) when the star is viewed magnetic pole-on. It is also worth noting that Prinja et al. (1990) measure a narrow absorption line component velocity $v_{NAC} \approx 350$ km s^{-1} at phase 0.1, comparable to the Doppler velocity of the X-ray lines discussed in § 5. In contrast, Stahl et al. (1996) measure a maximum edge velocity $v_{edge} \approx 2500$ km s^{-1}. The net result is that the confinement parameter for θ^1 Ori C is in the approximate range $5 \leq \eta_\star \leq 20$. The low terminal wind speed, $v_\infty \approx 510$ km s^{-1}, measured by Prinja et al. (1990) is lower than the escape velocity of θ^1 Ori C,
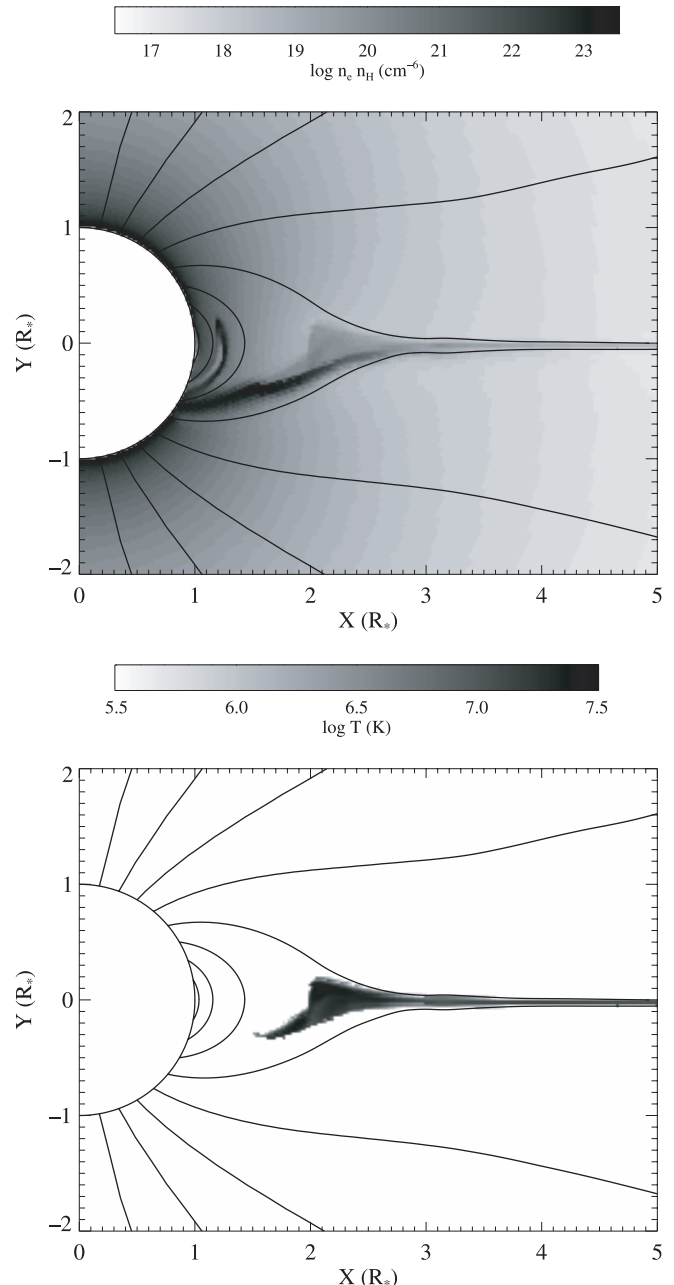

Fig. 5.—Snapshots from the 500 ks, slow-wind, two-dimensional MHD simulation of θ^1 Ori C, with corresponding magnetic field lines superposed. *Top*: Logarithm of the emission measure per unit volume, $\log n_e n_H$. *Bottom*: Logarithm of temperature, $\log T$. In this snapshot, obtained at simulation time $t = 375$ ks, material trapped in closed loops is falling back toward the stellar surface along field lines, forming a complex "snakelike" pattern. The regions of highest emission measure in the $1–100$ MK temperature range occur above and below the magnetic equator, close to $R \approx 2R_\star$. [*See the electronic edition of the Journal for a color version of this figure.*]

$v_{esc} \approx 1000$ km s^{-1}. Our $\eta_\star \approx 7.5$ model produces a 1470 km s^{-1} wind above the magnetic pole.

Starting from an initial time $t = 0$, when the dipole magnetic field is suddenly introduced into a smooth, steady, spherically symmetric, CAK wind, our MHD simulation follows the evolution through a total time interval, $t = 500$ ks, that is many characteristic wind flow times, $R_\star/v_\infty \approx 5$ ks. Figure 5 is a snapshot of the spatial distribution of log emission measure per unit volume (*top panel*) and log temperature (*bottom panel*) at a time, $t = 375$ ks, when material is falling back onto the photosphere along magnetic field lines (*solid lines*).

After introduction of the field, the wind stretches open the field lines in the outer region. In the inner region, the wind is channeled toward the magnetic equator by the closed field lines. Within these closed loops, the flow from opposite hemisphere collides to make strong, X-ray–emitting shocks. At early times, the shocks are nearly symmetric about the magnetic equatorial plane, like those predicted in the semianalytic, fixed-field models of Babel & Montmerle (1997b). Two-dimensional movies[12] of θ^1 Ori C show the evolution of density, temperature, and wind speed from the initially dipolar configuration.

Figure 5 shows, however, that the self-consistent, dynamical structure is actually much more complex. This is because once shocked material cools, its support against gravity by the magnetic tension along the convex field lines is inherently unstable, leading to a complex pattern of fall-back along the loop lines down to the star. As this infalling material collides with the outflowing wind driven from the base of a given loop line, it forms a spatially complex, time-variable structure, thereby modifying the location and strength of the X-ray–emitting shocks. When averaged over time, however, the X-ray emission appears to be symmetric and smooth.

It should be emphasized here that the implied time variability of shock structure and associated X-ray emission in this simulation is made somewhat artificial by the assumed two-dimensional, axisymmetric nature of the model. From a more realistic three-dimensional model (even without rotation), we expect the complex infall structure would generally become incoherent between individual loop lines at different azimuths (i.e., at different magnetic longitudes). As such, the azimuthally averaged X-ray emission in a realistic three-dimensional model is likely to be quite similar to the time-averaged value in the present model. A reliable determination of the expected residual level of observed X-ray variability in such wind-confinement models must await future three-dimensional simulations that account for the key physical processes setting the lateral coherence scale between loops at different azimuth. But based on the fine scale of magnetic structure in resolved systems such as the solar corona, it seems likely that this lateral coherence scale may be quite small, implying only a low level of residual variability in spatially integrated X-ray spectra.

Overall, we thus see that introduction of the initial dipole magnetic field results in a number of transient discontinuities that quickly die away. The wind in the polar region stretches the magnetic field into a nearly radial configuration and remains quasi-steady and smooth for the rest of the simulation. However, near the equatorial plane, where the longitudinal component of the magnetic field, B_θ, is large, the wind structure is quite complex and variable. In the closed field region within an Alfvén radius, $R \approx 2R_\star$, the field is nearly perpendicular to the magnetic equatorial plane and strong enough to contain the wind. The material from higher latitudes is thus magnetically channeled toward the equator and can reach velocities $v_\theta \approx 1000$ km s^{-1}.

Such high speeds lead to strong equatorial shocks, with postshock gas temperatures of tens of millions of degree within an extended cooling layer. The resulting cool, compressed material is then too dense to be supported by radiative driving, and so falls back onto the surface in a complex ''snakelike'' pattern (see Fig. 5). The equatorial material farther away from the surface gains the radial component of momentum from the channeled wind, eventually stretching the field lines radially. Eventually, the fields reconnect, allowing this material to break out. This dynamical situation provides two natural mechanisms for emptying the magnetosphere: gravitational infall onto the stellar surface and break-out at large radii.
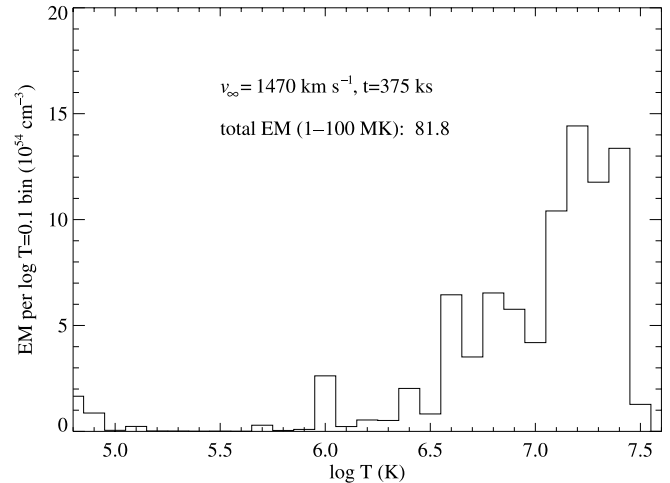
[12] See http://www.bartol.udel.edu/tloc.

FIG. 6.—Volume emission-measure distribution per log $T = 0.1$ bin, from the snapshot in Fig. 5. The MHD simulation is used to compute the emission-measure per unit volume per logarithmic temperature bin, then integrated over three-dimensional space assuming azimuthal symmetry about the magnetic dipole axis. The total simulated volume emission measure in the interval $6.0 \leq \log T < 8.0$ closely matches the total emission measure seen with the HETG in Table 6. The low-velocity wind ($v_\infty \approx 1470$ km s^{-1}) simulation in Fig. 5 also produces a slightly cooler distribution of shocks than observed. Full three-dimensional MHD simulations may be needed to resolve these discrepancies.

A key result here is that the bulk of the shock-heated plasma in the magnetosphere is moving slowly, implying very little broadening in the resulting X-ray emission lines. Most of the X-rays are produced in a relatively small region around $R \approx 2R_\star$ where the density of hot gas is high. Although the infalling and outflowing components are moving faster, much of the infalling material is too cool to emit X-rays, while the outflowing plasma's density is too low to produce very much X-ray emission.

To quantify these temperature and velocity characteristics, we postprocessed the results of these MHD simulations to produce an emission measure per unit volume at each two-dimensional grid point. Then, accounting for viewing geometry and occultation by the stellar photosphere, emission-line profiles and broadband X-ray spectra were generated for a number of viewing angles. In this procedure we account for the effects of geometry and occultation on line shapes and fluxes, but we neglect attenuation by the stellar wind and the dense equatorial outflows. While there is empirical evidence of some excess absorption in the magnetic equatorial plane (see § 5.3), the effect is much smaller than would be expected from a dense equatorial cooling disk, as in the Babel & Montmerle (1997b) model. Our MHD simulations indicate that an X-ray–absorbing cooling disk never has a chance to form, because of infall onto the photosphere and outflow along the magnetic equatorial plane.

Figure 6 plots the volume emission-measure distribution per log $T = 0.1$ bin for the snapshot in Figure 5. The MHD simulation is used to compute the emission measure per unit volume per logarithmic temperature bin, then integrated over three-dimensional space assuming azimuthal symmetry about the magnetic dipole axis.

The resulting synthesized X-ray emission lines are quite narrow, $\xi \leq 250$ km s^{-1}, with symmetric profiles that are only slightly blueshifted, $-100 \leq v_r \leq 0$ km s^{-1}. They are thus quite distinct from profiles expected from a wind outflow (Kramer et al. 2003b). The regions of highest emission measure are located close to the star, $R \approx 2R_\star$; the total volume emission measure (visible at rotational phase 0.0) exceeds 10^{56} cm^{-3}; the eclipse fraction is 20%–30%; and the temperature distribution

peaks at 20–30 MK, depending on the simulation snapshot. The resulting narrow-line profiles and hard X-ray spectra are in marked contrast to observed X-ray properties of supergiant O stars like ζ Pup (Kahn et al. 2001; Owocki & Cohen 2001; Ignace 2001; Ignace & Gayley 2002; Kramer et al. 2003a). But they match quite well the *Chandra* spectra of θ^1 Ori C reported in this paper and of a handful of young OB stars like τ Scorpii (Cohen et al. 2003) and the other components of θ Ori (Schulz et al. 2003).

5. X-RAY SPECTRAL DIAGNOSTICS

In the context of the picture of θ^1 Ori C that we have painted in the last two sections—a young hot star with a strong wind and a tilted dipole field that controls a substantial amount of circumstellar matter—we now discuss the X-ray spectral diagnostics that can further elucidate the physical conditions of the circumstellar matter and constrain the physics of the magnetically channeled wind. The reduction and analysis of the four *Chandra* grating observations have been described in § 2, and here we discuss the diagnostics associated with (1) the line widths and centroids, which contain information about plasma dynamics; (2) the line ratios in the helium-like ions, which are sensitive to the distance of the X-ray–emitting plasma from the stellar photosphere; and (3) the abundance, emission-measure, temperature, and radial-velocity variations with viewing angle, which provide additional information about the plasma's geometry.

5.1. *Emission Line Widths and Centroids*

The Doppler broadening of X-ray emission lines provides direct information about the dynamics of the hot plasma that is ubiquitous on early-type stars. For these stars, with fast, dense radiation-driven winds, X-ray line widths and profiles have been used to test the general idea that X-rays arise in shock-heated portions of the outflowing stellar winds, as opposed to magnetically confined coronal loops, as is the case in cool stars. Single O supergiants thus far observed with *Chandra* and *XMM-Newton* generally show X-ray emission lines that are broadened to an extent consistent with the known wind velocities (Waldron & Cassinelli 2001; Kahn et al. 2001; Cassinelli et al. 2001), namely, $v_{\rm HWHM} \approx 1000$ km s^{-1}, which is roughly half of v_∞, as would be expected for an accelerating wind. Very early B stars, although they also have fast stellar winds, show much less Doppler broadening (Cohen et al. 2003). Some very late O stars, such as δ Ori (Miller et al. 2002), and unusual Be stars such as γ Cas (Smith et al. 2004), show an intermediate amount of X-ray line broadening. It should be noted that although short-lived bulk plasma flows are seen during individual flare events on the Sun, cool stars do not show highly Doppler broadened X-ray emission lines in *Chandra* or *XMM-Newton* grating spectra. It should also be noted that with high enough S/N, *Chandra* HETGS data can be used to measure Doppler broadening of less than 200 km s^{-1} (Cohen et al. 2003).

In addition to a simple analysis of X-ray emission line widths, analysis of the actual profile shapes of Doppler-broadened lines can provide information about the dynamics and spatial distribution of the X-ray–emitting plasma and the nature of the continuum absorption in the cold wind component (MacFarlane et al. 1991; Ignace 2001; Owocki & Cohen 2001; Cohen et al. 2002; Feldmeier et al. 2003; Kramer et al. 2003b). These ideas have been used to fit wind-shock X-ray models to the *Chandra* HETGS spectrum of the O4 supergiant ζ Pup (Kramer et al. 2003a). This work, and qualitative analyses of observations of other O stars, indicates that wind attenuation of X-rays is significantly less important than had been assumed in O stars, but that generally, the wind-shock framework for understand-ing X-ray emission from early-type stars is sound, at least for O-type supergiants.

For θ^1 Ori C, where the magnetic field plays an important role in controlling the wind dynamics, the specific spherically symmetric wind models of X-ray emission line profiles mentioned above may not be applicable. However, the same principles of inverting the observed Doppler line profiles to infer the wind dynamics and effects of cold-wind absorption and stellar occultation are, in principle, applicable to θ^1 Ori C as well, if an appropriate quantitative model can be found.

In their work on the magnetic field geometry of θ^1 Ori C, Donati et al. (2002) calculated several quantitative line profiles based on the (rigid-field) MCWS model and various assumptions about the spatial extent of the magnetosphere, the wind mass-loss rate, and the optical thickness of the "cooling disc" that is thought to form in the magnetic equator. Donati et al. (2002) examined the Babel & Montmerle model for five sets of stellar/disk parameters. Their model 3 produces relatively narrow, symmetric X-ray lines (as observed), and requires very little absorption in the cooling disk. The location of the X-ray emitter, its emission measure, the X-ray line profiles, and the time variability can be correctly predicted by accounting for the interaction between the wind and the magnetic field.

Line width and profile determinations for θ^1 Ori C have already been made using the two GTO *Chandra* grating spectra. Unfortunately, in the literature there are two divergent results based on the same data. Schulz et al. (2000) claimed that the emission lines in the HETGS data from the ObsID 3, 31 October 1999, observation were broad (mean FWHM velocity of 771 km s^{-1} with some lines having FWHMs as large as 2000 km s^{-1}). In a second paper, based on both ObsID 3 and 4 data sets, Schulz et al. (2003) claimed that all the lines, with the exception of a few of the longest wavelength lines, were unresolved in the HETGS spectra. This second paper mentions a software error and also the improper accounting of line blends as the cause for the discrepancy. However, as we show below, the results of modest, but nonzero, line broadening reported in the first paper (Schulz et al. 2000) are actually more accurate.

Schulz et al. (2003) detected 81 lines in the combined HEG/ MEG spectra θ^1 Ori C from ObsID 3 and 4. Although 82 lines are listed here in Table 2 of this paper, 35 lines have no flux errors, signifying that they were blended with other brighter lines. Hence, Schulz et al. (2003) detect more lines, but at lower S/N. Generally, Schulz et al. (2003) find line fluxes comparable to those in Table 2, because ObsID 3 and 4 were obtained at intermediate phases, and the combined HEG and MEG spectra presented here are the sum of spectra obtained at low, inter-mediate, and high phases.

With the detailed analysis we carried out and described in § 2, we find finite, but not large, line widths, as indicated in Table 2. The lines are clearly resolved, as we show in Figures 7 and 8, in which two strong lines, one in the HEG and one in the MEG, are compared to intrinsically narrow models, to Doppler-broadened models, and also to data from a late-type star with narrow emission lines.

We took a significant amount of care in deriving the line widths, fitting all lines in a given complex and carefully ac-counting for continuum emission. We fit each of the four ob-servations separately, but generally find consistent widths from observation to observation, as we discuss below. In Figure 9, the Doppler width $v_{\rm D}$ of each line (*open circles*) is plotted versus the peak $\log T$ of that line. The rms turbulent velocities ξ are plotted as filled diamonds. The Doppler widths are slightly higher than the rms velocities because the Doppler width includes the effects of thermal broadening. The velocities do not appear to
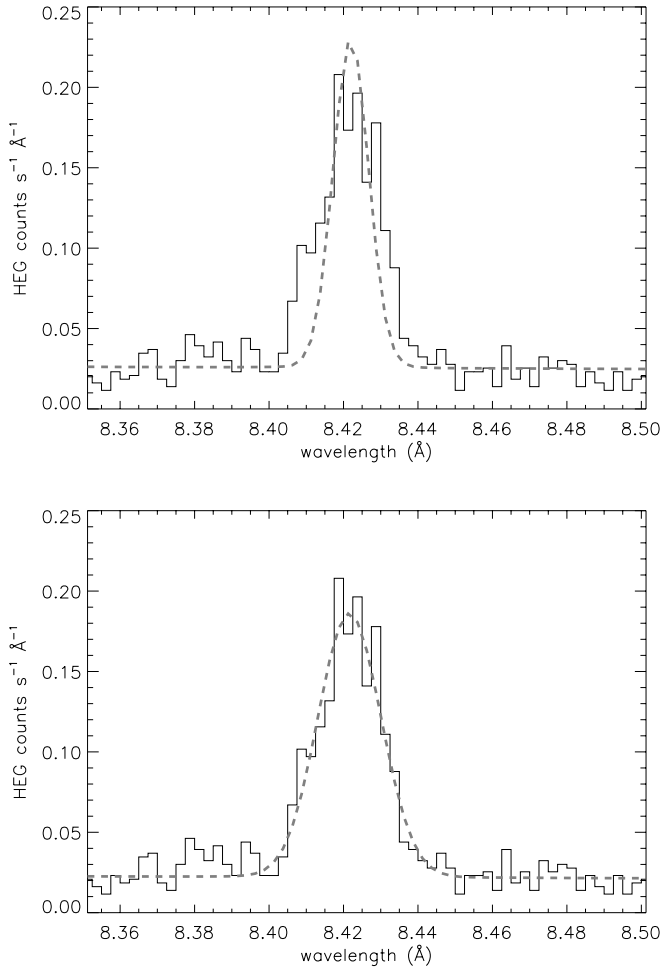
Fig. 7.—Mg Lyα line in the combined *Chandra* HEG spectrum from all four observations (*solid histogram, both panels*). A model with only thermal broadening ($v_{\text{th}} = 104$ km s^{-1}; *dashed line, top panel*) is much narrower than the observed profile. A Gaussian line model with thermal and turbulent broadening due to bulk motion ($\xi = 328$ km s^{-1}; *dashed line, bottom panel*) provides a better fit to the data.
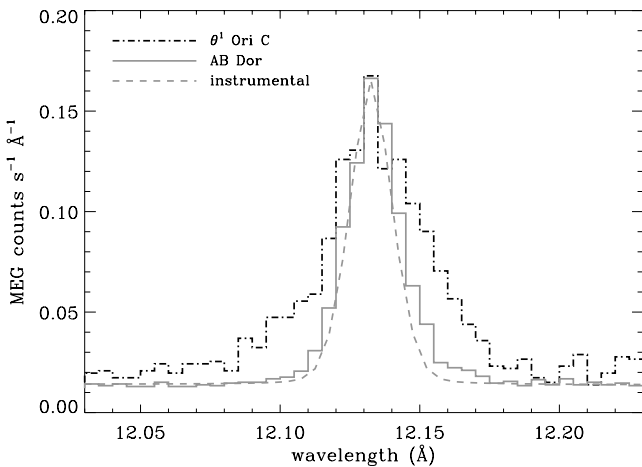

Fig. 8.—Ne Lyα line in the combined *Chandra* MEG spectrum from all four observations of θ^1 Ori C (*solid histogram*) compared to the same line seen in the MEG spectrum of the active young K-type dwarf, AB Doradus (*dash-dotted histogram*). A delta function convolved with the MEG instrumental response (*dashed line*) is also shown for comparison. The θ^1 Ori C line is clearly broader than both the narrow line or the AB Dor line.
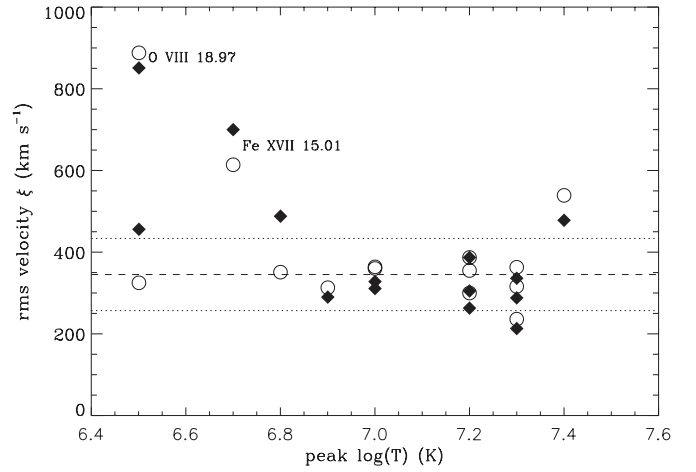
Fig. 9.—Line widths for the strongest lines in the *Chandra* spectra plotted against the temperature of peak line emissivity, taken from APED. The open circles represent the Doppler width as measured by SHERPA. The filled diamonds represent the rms velocity as measured by ISIS. The mean rms velocity and standard deviations of these lines are indicated by the horizontal lines. Note that two of the lines formed in the coolest plasma are significantly broader than the mean, but most of the lines have nonthermal line widths of a 250–450 km s^{-1}.

depend on temperature; however, there are two anomalous line profiles. The O VIII Lyα at 18.97 Å ($\xi \approx 850$ km s^{-1}) and Fe XVII at 15.01 Å ($\xi \approx 700$ km s^{-1}) are substantially broader than any of the other lines. Excluding these two lines, we find a mean $v_D = 351 \pm 72$ km s^{-1} and a mean $\xi = 345 \pm 88$ km s^{-1}. Because O VIII and Fe XVII tend to form at lower temperatures ($T \approx 5 \times 10^6$), the two broader lines could represent cooler plasma formed by the standard wind instability process. Approximately 80% of the total emission measure is in the hotter 30 MK plasma. For lines formed in this hotter plasma, the Doppler broadening is substantially lower than the wind velocity. The modeled line widths from the MHD simulations, however, are quantitatively consistent with the results derived from the data.

The line widths we derive from the data are relatively, but not totally, narrow, and they are also approximately constant as a function of rotational phase and magnetic field viewing angle.
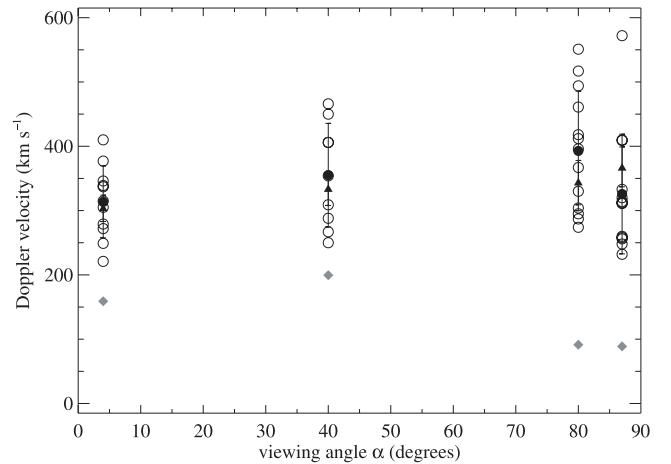

Fig. 10.—Line widths for the strongest lines in the *Chandra* spectra (*open circles*) at each of our four observations. The filled circles are the mean measured line widths and the error bars are the standard deviations of the mean values. The gray diamonds are the theoretical predictions based on the MHD simulations. The velocity widths plotted here are the Doppler width components, v_D, as described in § 2. Note that the observed lines are somewhat broader than predicted by the MHD simulations, but substantially less broad than expected from line-driven shocks in the wind.
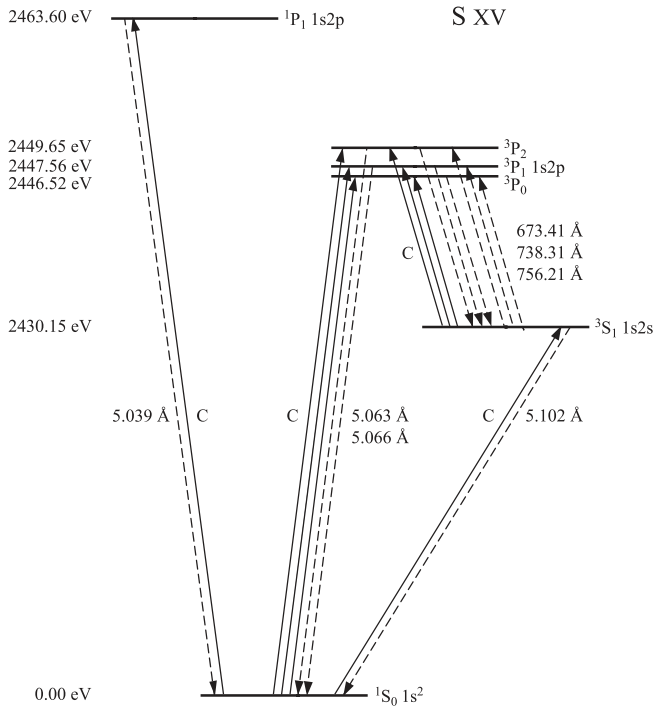
FIG. 11.—Energy-level diagram for S XV, based on the O VII diagram of Gabriel & Jordan (1969). Collisional excitations (*C*) are shown as upward pointing solid lines; radiative decays are shown as downward pointing dashed lines; photoexcitations are shown as upward pointing dashed lines. APED level energies and observed transition wavelengths are also shown. Electrons are excited out of the metastable $^3S_1$ state by collisions at high density and by radiation close to a hot photosphere.

We show these results in Figure 10. This is somewhat surprising in the context of the MCWS model as elucidated by Babel & Montmerle (1997b) and Donati et al. (2002), in which the pole-on viewing angle is expected to show more Doppler broadening, as the shock-heated plasma should be moving toward the magnetic equatorial plane along the observer's line of sight. However, as we show in § 4, the full numerical simulations predict nonthermal line widths of 100–250 km s^{-1}. In Figure 10 we show the Doppler velocity from a simulation with a stable magnetosphere (cf. Fig. 5) as gray filled diamonds.

Finally, the dynamics of the shock-heated plasma in the MCWS model might be expected to lead to observed line centroid shifts with phase or viewing angle. This would be caused by occultation of the far side of the magnetosphere by the star or by absorption in the cooling disk (see Donati et al. 2002).

As predicted by the MHD simulations, the data show line centroids very close to zero velocity at all viewing angles. Note, however, that the global fits discussed in § 5.3 show evidence for a small viewing-angle dependence.

5.2. Helium-like Forbidden-to-Intercombination Line Ratios

The ratio of forbidden-to-intercombination (f/i) line strength in helium-like ions can be used to measure the electron density of the X-ray–emitting plasma and/or its distance from a source of far-UV radiation, such as the photosphere of a hot star (Blumenthal et al. 1972). Figure 11 is an energy-level diagram for S XV similar to the one for O VII first published by Gabriel & Jordan (1969). It shows the energy levels (eV) and transition wavelengths (Å) from APED of the resonance ($^1P_1 \rightarrow ^1S_0$), intercombination ($^3P_{2,1} \rightarrow ^1S_0$), and forbidden ($^3S_1 \rightarrow ^1S_0$) lines. Aside from the usual ground-state collisional excitations (*solid lines*) and radiative decays (*dashed lines*), the metastable $^3S_1$ state can be depopulated by collisional and/or photoexcitation to the ^3P states. In late-type stars, the f/i ratios of low-Z ions such as N VI and O VII are sensitive to changes in electron density near or above certain critical densities (typically in the 10^{12} cm^{-3} regime). Higher Z ions have higher critical electron densities usually not seen in normal (nondegenerate) stars. Kahn et al. (2001) have used the f/i ratios of N VI, O VII, and Ne IX and the radial dependence of the incident UV flux to determine that most of the emergent X-rays from the O4 supergiant ζ Pup were formed in the far wind, consistent with radiatively driven wind shocks.

In our observations of θ^1 Ori C, the He-like lines of Fe XXV, Ca XIX, Ar XVII, S XV, Si XIII, and Mg XI were detected at all phases. However, accurate f/i ratios cannot be determined for all ions. The resonance and intercombination lines of Fe XXV at 1.850 Å and Ca XIX at 3.177 Å are blended in the HEG, and weak or nonexistent in the MEG. Similarly, Ne IX at 13.447 Å and O VII at 21.602 Å are weak or nonexistent in the HEG.

Derived forbidden-to-intercombination (f/i) and forbidden+ intercombination-to-resonance ($f + i$)/r ratios are listed in Table 4. The Mg XI, Ne IX, and O VII forbidden lines are completely suppressed via far-UV photoexcitation of the $^3S_1$ upper level, while the forbidden lines of Si XIII, S XV, and Ar XVII are partially suppressed. Figure 12 shows the He-like line complexes of Ar XVII, S XV, Si XIII, and Mg XI with their best-fit models. The forbidden lines of O VII and Ne IX (not shown in Fig. 12) are completely suppressed.

The Ar XVII forbidden line at 3.994 Å is blended with S XVI Lyβ at 3.990 and 3.992 Å and S XV at 3.998 Å. Based on the ISIS abundances and emission measures (see § 5.3 below), APED predicts that only 26% of the HEG line flux comes from the Ar XVII f line. In the above case, the f/i ratio is highly uncertain and strongly model dependent, making the use of this line ratio problematic. The Si XIII f line at 6.740 Å is blended with the Mg XII Lyγ doublet at 6.738 Å. Similarly, we estimate that the Mg XII doublet's flux is approximately 11.8 × 10^{-6} photons cm^{-2} s^{-1}, approximately 38% of the flux at 6.740 Å. Assigning the remaining flux to the Si XIII f line results in $f/i = 0.98$; we have assigned a large 30% uncertainty in Table 4 because of the blending problem.

TABLE 4
He-like Line Diagnostics

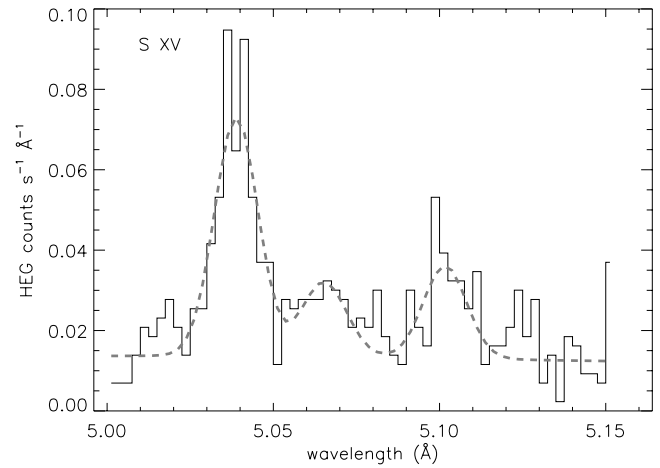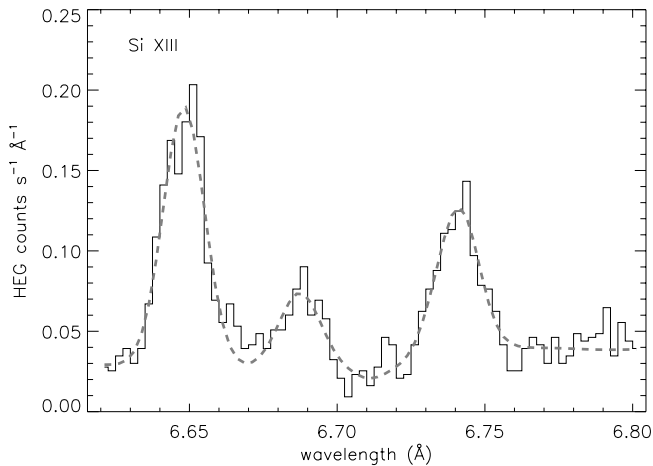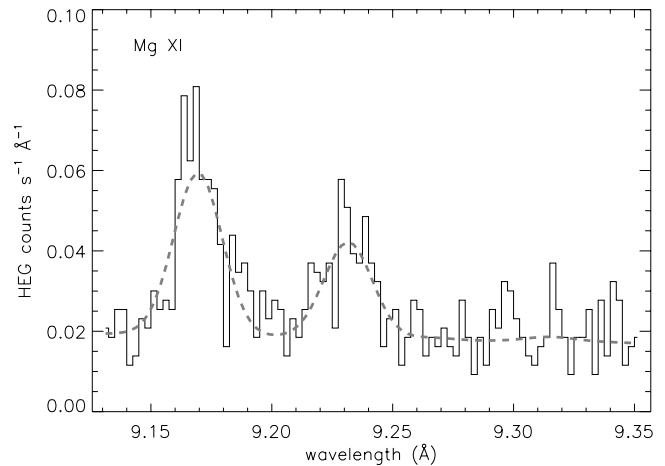| Ion	$^3P_2 \rightarrow ^3S_1$ (Å)	$^3P_1 \rightarrow ^3S_1$ (Å)	r (10^{-6} photons cm^{-2} s^{-1})	i (10^{-6} photons cm^{-2} s^{-1})	f (10^{-6} photons cm^{-2} s^{-1})	R (f/i)	σ_R	G [$(f+i)/r$]	σ_G
Ar XVII	560	640	13.02	6.84	12.37	1.81	0.37	1.47	0.36
S XV	673	783	50.53	15.93	21.92	1.38	0.22	0.75	0.08
Si XIII	815	865	61.40	19.44	18.98	0.98	0.30	0.63	0.07
Mg XI	977	1034	28.89	17.37	1.36	0.08	0.07	0.65	0.07
Ne IX	1248	1273	33.29	26.37	0.41	0.02	0.11	0.83	0.19
O VII	1624	1638	16.98	14.42	0.00	0.00	0.20	0.85	0.71
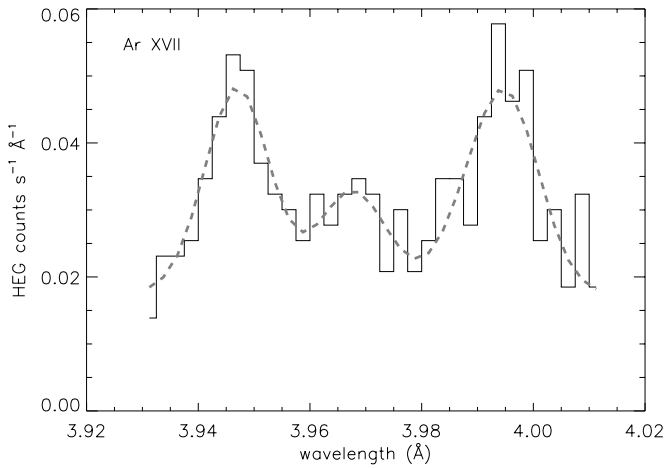
FIG. 12.—Ar XVII, S XV, Si XIII, and Mg XI He-like line complexes. In each panel, the data (*solid histogram*) and model (*gray dashed line*) of the resonance (*r*), intercombination (*i*), and forbidden (*f*) lines are shown. Note that as atomic number increases from $Z = 12$ (Mg XI) to $Z = 18$ (Ar XVII), the relative strength of the forbidden line to the intercombination line increases. The Si XIII *f* line is blended with a Mg XII line. The other detected He-like lines were not used for the diagnostic analysis: Ca XIX was too weak, and the Fe XXV *f* and *i* lines were not resolved.

This leaves us with f/i measurements for Mg XI, S XV, and Si XIII. We take the Mg forbidden line to be undetected (the fit result in Table 4 shows that it is just barely detected at the 1 σ level). The sulfur f/i value is quite well constrained, however, and lies somewhere between the two limits (generally referred to as "high-density" and "low-density," reflecting the traditional use of this ratio as a density diagnostic in purely collisional plasmas).

Of course, the photospheric emergent fluxes must be known at the relevant UV wavelengths for the f/i ratio to determine the location of the X-ray–emitting plasma. The Mg XI, Si XIII, and S XV photoexcitation wavelengths are listed in Table 4. The 1034 Å flux has been measured using archival *Copernicus* spectra. For the fluxes short of the Lyman limit at 912 Å, where we have no data and for which non-LTE model atmospheres and synthetic spectra have not been published, we scaled the flux from a 45,000 K blackbody (the hot model in Table 3). We computed the f/i ratios using the PrismSPECT non-LTE excitation kinematics code (MacFarlane et al. 2003). For each line complex, we set up a model atom with several dozen levels for each ion using oscillator strengths and transition rates custom-computed using Hartree-Fock and distorted-wave methodologies. The resulting values were checked against data from the literature. We include collisional and radiative coupling among

most levels in the model atom, and specifically include photoexcitation between the $^3S_1$ and ^3P levels driven by photospheric radiation.

The results of this modeling for Mg XI and S XV are shown in Figure 13, where the solid lines represent f/i as a function of electron density for a range of radii from 1 to 200 $R_\star$. The dashed line in Figure 13 (*top*) is the Mg XI upper limit, indicating an upper limit to the formation radius $R \leq 1.7R_\star$. The dashed lines in Figure 13 are the S XV 1 σ upper and lower bounds, indicating a formation radius in the range $1.2R_\star \leq R \leq 1.5R_\star$. The resulting bounds from Si XIII are consistent with S XV. Of course, it is a simplification to assume that all of the plasma (even for a given element or ion stage) is at a single radius. The formation radii we have derived should thus be thought of as an emission-measure–weighted mean. In any case, it is clear that the hot plasma in the circumstellar environment of θ^1 Ori C is quite close to the photosphere. We note that there is no variation in the average formation radius among the four separate phase observations. We also note that these results are comparable to those found by Schulz et al. (2003) based on the earlier two data sets.

5.3. *Emission-Measure and Abundance Variability*

There are several additional diagnostics that involve analysis of not the properties of single lines, but the X-ray spectrum as a
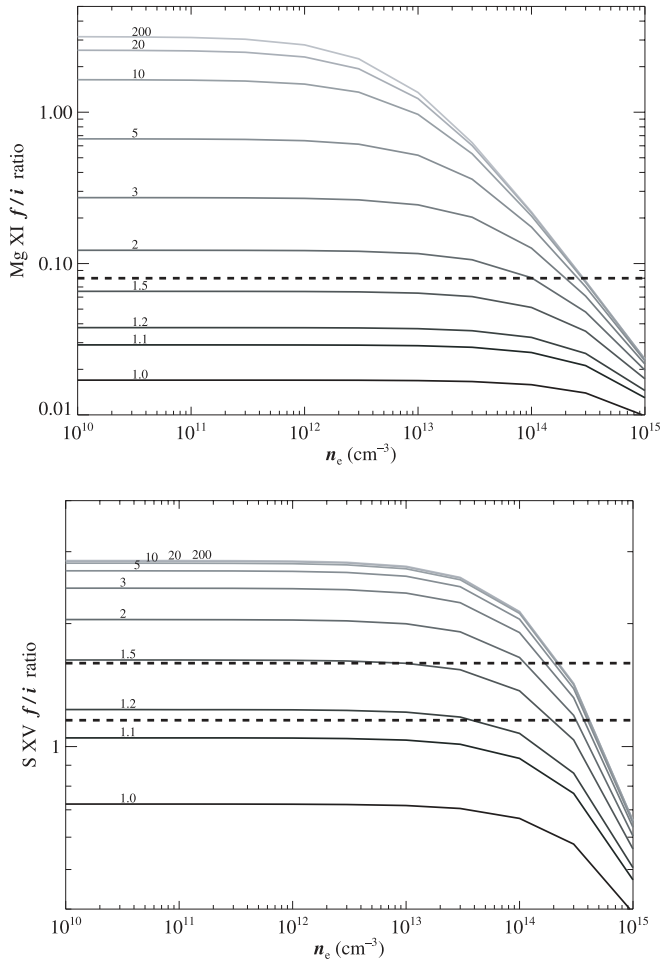
Fig. 13.—He-like f/i ratio vs. n_e at various radii from $1R_\star$–$200R_\star$, assuming a 45,000 K photosphere, for Mg XI (*top*) and S XV (*bottom*). The measured f/i upper and lower bounds from Table 4 are shown as dashed lines. The Mg XI, Si XIII, and S XV suggest a formation radius $1.2R_\star \leq R \leq 1.5R_\star$.

dances do not deviate significantly from solar, although Fe is well below solar and several intermediate atomic number elements are slightly above solar.

The HEG/MEG spectra for each observation were fit with a variable-abundance, two-temperature ISIS plasma model with radial velocity and turbulent (rms) velocity as free parameters (see Table 6), with a single column density parameter, N_H. We tried fitting the individual and combined spectra with 2, 5, and 21 temperature APEC models with solar and nonsolar abundances. No solar-abundance model can adequately fit the continuum and emission lines. The 5 and 21 temperature component models do not provide appreciably better fits than the two-temperature nonsolar abundance model. Although plasma at a number of temperatures may be present, it is not possible to accurately fit so many free parameters with moderate-S/N HETG data.

Schulz et al. (2003) used a six-temperature, variable abundance APEC plasma model to fit the combined HEG/MEG spectra from ObsID 3 and 4. They find $N_H \approx 5 \times 10^{21}$ cm^{-2}, subsolar Fe, Ni, O, and Ne, and approximately solar abundances of other elements, again consistent with our results in Table 6. Their Figure 7, however, suggests a phase dependence in the six-temperature emission-measure distribution, which we cannot confirm. We point out, however, that the 1 σ error envelope in their emission-measure distributions overlap significantly. The emission measures in Table 6 for phases 0.38 and 0.84 appear to fit within both EM envelopes in Figure 7 of Schulz et al. (2003).

The visible emission measure decreases by 36% from X-ray maximum to minimum, suggesting that a substantial fraction of the X-ray–emitting region is occulted by the star at high viewing angles. Comparison between the observed data and the MHD simulations show that the agreement is quite good, in terms of both the overall volume emission measure and its temperature distribution.

As has previously been shown (Gagné et al. 1997; Babel & Montmerle 1997b; Donati et al. 2002), the phase dependence of the X-ray spectrum provides information about the extent and location of the X-ray emission and absorption in the wind and disk. There are no large, systematic spectral variations at the four phases observed with *Chandra*. For example, the soft X-ray portion of the MEG is not more absorbed than the hard X-ray portion, suggesting that the variability is not primarily caused by absorption in the disk or by a polar wind. Rather, it appears that most of the variability is caused by occultation of the X-ray emitter by the stellar photosphere as the magnetically confined region rotates every 15.4 days.

whole. The global thermal model fitting with ISIS described in § 2 yields abundance and emission-measure information, while the line flux values taken as an ensemble can be analyzed for phase or viewing-angle dependence. Detailed descriptions of these analyses have already been presented § 2, so here we simply present the results.

The elemental abundances derived from the two different fitting methods are reported in Table 5. Most elemental abun-

TABLE 5
AVERAGE ELEMENTAL ABUNDANCES FOR θ^1 ORI C

ELEMENT	GLOBAL FIT		LINE FIT		LINES USED FOR FIT
	Abundance	σ	Abundance	σ	
O......................	0.76	0.04	0.76	0.08	O VIII λ18.98
Ne....................	0.69	0.02	1.04	0.05	Ne X λ12.13
Mg..................	0.81	0.02	0.94	0.02	Mg XII λ8.42
Si	1.18	0.02	1.11	0.02	Si XIV λ6.18
S	1.40	0.05	1.22	0.06	S XVI λ4.73
Ar	1.28	0.13	1.48	0.17	Ar XVII λ3.95
Ca	1.12	0.18	1.72	0.19	Ca XIX λ3.18
Fe....................	0.60	0.01	0.62	0.06	Fe XVII $\lambda\lambda$15.01, 16.78; Fe XIX λ15.01; Fe XX $\lambda\lambda$15.00, 15.02; Fe XXII λ11.77;
					Fe XXIII $\lambda\lambda$10.98, 11.02, 11.74; Fe XXIV $\lambda\lambda$10.62, 11.03, 11.18; Fe XXV λ1.85

NOTE.—Abundances relative to solar (Anders & Grevesse 1989). The combined HEG and MEG first-order spectra were fit using a multitemperature APED plasma model in ISIS.

TABLE 6
GLOBAL ISIS FIT PARAMETERS AND 90% CONFIDENCE LIMITS

Parameter	ObsID 2567 ($\phi = 0.01$, $\alpha = 4°$)	ObsID 3 ($\phi = 0.84$, $\alpha = 40°$)	ObsID 4 ($\phi = 0.38$, $\alpha = 80°$)	ObsID 2568 ($\phi = 0.47$, $\alpha = 87°$)	Average
L_X[a] (10^{33} ergs s^{-1})...........	1.13 ± 0.06	1.00 ± 0.05	0.77 ± 0.04	0.75 ± 0.04	1.03 ± 0.05
N_H (10^{21} cm^{-2})................	$4.51^{+0.17}_{-0.17}$	$4.54^{+0.19}_{-0.17}$	$4.58^{+0.34}_{-0.29}$	$4.93^{+0.27}_{-0.23}$	$4.61^{+0.13}_{-0.11}$
EM_1 (10^{54} cm^{-3})	$14.3^{+1.1}_{-0.9}$	$13.6^{+0.9}_{-0.9}$	$9.7^{+1.0}_{-1.2}$	$10.3^{+0.9}_{-0.2}$	$13.7^{+0.6}_{-0.5}$
T_1 (10^6 K)	$8.4^{+0.2}_{-0.1}$	$8.4^{+0.2}_{-0.1}$	$8.4^{+0.3}_{-0.2}$	$8.5^{+0.2}_{-0.2}$	$8.5^{+0.1}_{-0.1}$
EM_2 (10^{54} cm^{-3})	$66.2^{+1.0}_{-1.0}$	$56.5^{+0.9}_{-0.8}$	$43.3^{+1.1}_{-1.1}$	$41.3^{+0.8}_{-0.9}$	$58.5^{+0.6}_{-0.6}$
T_2 (10^6 K)	$29.2^{+0.4}_{-0.5}$	$30.1^{+0.5}_{-0.5}$	$33.6^{+1.2}_{-1.2}$	$33.6^{+1.0}_{-1.0}$	$32.6^{+0.5}_{-0.5}$
ξ (km s^{-1}).......................	303^{+21}_{-20}	333^{+21}_{-25}	343^{+35}_{-34}	366^{+33}_{-29}	348^{+16}_{-14}
v_r (km s^{-1})......................	-75^{+10}_{-10}	-66^{+12}_{-9}	19^{+19}_{-18}	93^{+16}_{-13}	-31^{+10}_{-5}

[a] L_X is the unabsorbed 0.5–10 keV (1.25–25 Å) X-ray luminosity assuming $d = 450$ pc.

That said, there does a appear to be a small increase in column density when the disk is viewed nearly edge-on. Figure 14 shows the ISIS parameters, N_H (*top curve, right axis*) and radial velocity (*bottom curve, left axis*), as a function of viewing angle. The excess column density, $N_H \approx 5 \times 10^{20}$ cm^{-2}, would arise as a result of increased outflow in the magnetic equatorial plane. Because increased column density and increased temperature harden the predicted X-ray spectrum in somewhat similar ways, we consider the column density variability as a tentative result. We point out that X-ray absorption toward θ^1 Ori C occurs in the ISM, in the neutral lid of the Orion Nebula, in the ionized cavity, and in the stellar wind. The Wisconsin absorption model for cold interstellar gas yields a single column density parameter, which does not take into account the ionization fraction, temperature, and abundance of these absorption components.

The measured radial velocities at viewing angles 4° (pole-on), 39°, 80°, and 87° (edge-on) were -75 ± 10, -66^{+12}_{-9}, 19^{+19}_{-18}, and 93^{+16}_{-13} km s^{-1}, respectively. Systematic line shifts were not detected in individual line complexes (see § 5.1) because the uncertainty in the centroid velocity of a single line is higher than its uncertainty based on a large number of lines. For instance, the 1 σ uncertainty at each ObsID in the line centroid of Fe XVII λ15.014 is approximately 50 km s^{-1}.

The simulations predict no significant blueshifts or redshifts at any viewing angle. As a result, the -75 km s^{-1} blueshift at

low viewing angle and the $+93$ km s^{-1} redshift at high viewing angle seen in Figure 11, if real, may lead to further improvements of the model. The two-dimensional MHD simulations show that the hot plasma is constantly moving, sometimes falling back to the photosphere in one hemisphere or the other, at other times expanding outward in the magnetic equatorial plane following reconnection events. Because the four *Chandra* observations were obtained months or years apart, the radial velocity variations may reflect the stochastic nature of the X-ray production mechanism or persistent flows of shock-heated plasma.

Although small, the X-ray line shifts nicely match the C IV, N V, and Hα emission components discussed by Smith & Fullerton (2005). In this picture, material falling back onto the photosphere along closed magnetic field lines produces redshifted emission when viewed edge-on. The blueshifted X-ray and Hα emission seen at low viewing angles (pole-on, $\phi = 0$) would be produced by (1) the same infalling plasma viewed from an orthogonal viewing angle and/or (2) material in the outflowing wind. Smith & Fullerton (2005) argue that a polar outflow probably cannot produce the observed levels of Hα and He II λ4686 emission, thereby preferring the infall scenario.

If pole-on blueshifts in the X-ray lines are persistent, this suggests asymmetric infall toward the north (near) magnetic pole. Such blueshifts could be caused by an off-centered oblique dipole. The blueshifts might also be caused by absorption of the red emission in the far hemisphere by the cooler postshock gas. However, this would produce weaker X-rays at pole-on phases. Since stronger X-ray emission is observed at pole-on phases, asymmetric infall provides a better explanation for the blueshifted Hα and X-ray line emission. Repeated observations at pole-on and edge-on phases are needed to confirm this result.

6. DISCUSSION

The high-resolution X-ray spectroscopy covering the full range of magnetospheric viewing angles adds a significant amount of new information to our understanding of the high-energy processes in the circumstellar environment of θ^1 Ori C, especially when interpreted in conjunction with data from other wavelength regions and our new MHD numerical simulations. As the simplified MCWS modeling (Babel & Montmerle 1997b; Donati et al. 2002) indicated and our detailed MHD simulations confirmed, the magnetically channeled wind model can produce the right amount of X-rays and roughly the observed temperature distribution in the X-ray–emitting plasma. The two new *Chandra* observations we report on in this paper reinforce the global spectral information already gleaned from the two GTO observations. In addition, the better phase coverage now shows that the modulation of the X-rays is quite gray, indicating
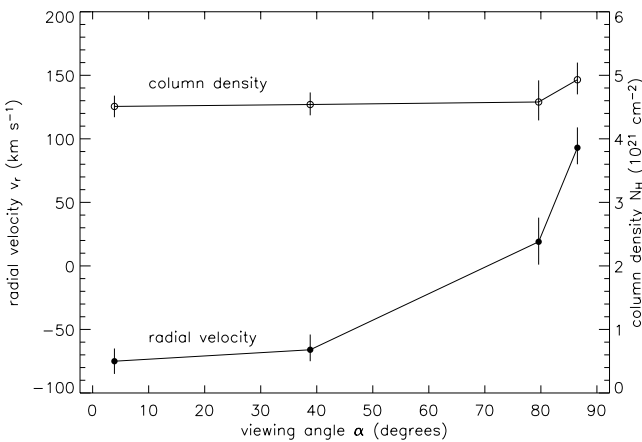

FIG. 14.—HEG/MEG spectra, showing slight changes in radial velocity (*left axis, filled circles*) and column density (*right axis, open circles*) from observation to observation. At low viewing angles (pole-on), the X-ray lines are slightly blueshifted; at high viewing angles (disk-on), the lines are redshifted, with a hint of excess absorption from ionized gas in the disk. The increased absorption may indicate outflowing wind material in the magnetic equatorial plane. The redshifts and blueshifts may indicate obliquely infalling material seen from various viewing angles.

that occultation by the star at phases when our view of the system is in the magnetic equatorial plane is the primary cause of the overall X-ray variability. Incidentally, the fact that the reduction in the flux is maximal at $\phi = 0.5$ confirms the reassessment of field geometry by Donati et al. (2002).

The fractional decrease in the observed flux of roughly 35%, interpreted in the context of occultation, indicates that the X-ray–emitting plasma is quite close to the photosphere: $1.2R_\star \leq R \leq 1.4R_\star$. This result is completely consistent with the observed Mg XI, Si XIII, and S XV f/i values, which together indicate $1.2R_\star \leq R \leq 1.5R_\star$, i.e., between 0.2 and 0.5 stellar radii above the photosphere. The MHD simulations we have performed also show the bulk of the very hot emission measure to be, on average, within $2R_\star$.

We see evidence for slightly enhanced attenuation at large viewing angles (nearly edge-on) as a result of wind material channeled into the magnetic equatorial plane. We should point out that the infall (in the closed-field region) and outflow (in the open-field region) means that a dense, X-ray absorbing, cooling disk does not form in the equatorial plane.

The X-ray emission lines seen in the *Chandra* spectra are well resolved, but relatively narrow, and show small (<100 km s^{-1}) centroid shifts. Although the two-dimensional MHD simulations indicate little or no line shifts on average, the small observed shifts (also seen in Hα) may reflect the stochastic nature of the infall onto the star. If the blueshifts at pole-on phases are persistent, they may indicate an asymmetry in the magnetic/wind geometry.

The line widths in the simulations are even narrower than those seen in the data. But this is, perhaps, not too surprising, as the simulations do not include the deshadowing instability that can lead to shock heating in the bulk wind. Some radiatively driven X-ray production in the cooler ($T \approx 6 \times 10^6$ K) wind shocks was suggested by Schulz et al. (2003) and may explain the larger widths of the Fe XVII and O VIII lines. Furthermore, fully three-dimensional simulations may reveal additional turbulence or other bulk motions.

7. CONCLUSIONS

The magnetically channeled wind shock model for magnetized hot stars with strong line-driven winds provides excellent agreement with the diagnostics from our phase-resolved *Chandra* spectroscopy of θ^1 Ori C. The modest line widths are consistent with the predictions of our MHD simulations. The X-ray light curve and He-like f/i values indicate that the bulk of the X-ray–emitting plasma is located at approximately $1.5R_\star$, very close to the photosphere, which is also consistent with the MHD simulations of the MCWS mechanism. The simulations also correctly predict the temperature and total luminosity of the X-ray–emitting plasma. We emphasize that the only inputs to the MHD simulations were the magnetic field strength, effective temperature, radius, and mass-loss rate of θ^1 Ori C, all of which are fairly well constrained by observation.

Although the original explorations of the MCWS mechanism indicated that there might be significant viewing angle dependencies in some of these diagnostics, the numerical simulations by and large do not predict them, and they are generally not seen in the data. Spatial stratification of the very hottest plasma might explain the slight wavelength dependence of the viewing angle variability of the X-ray flux.

The new MHD simulations we present for θ^1 Ori C are similar to the original calculations by ud-Doula & Owocki (2002), but the more accurate treatment of the energy equation makes for some modest changes, and allows for a direct prediction of its X-ray emission properties. Future, fully three-dimensional simulations might show even better agreement with the data if different longitudinal sectors of the magnetosphere exhibit independent dynamics. But the addition of rotation into the dynamical equations of motion probably is not important for this star and seems to be unnecessary for reproducing the observations.

The red and blue wings of the C IV and N V UV resonance-lines, the optical H I Balmer and He II lines, and small centroid velocity shifts in the X-ray lines may point to more complicated, episodic infall and/or mass-loss.

As was pointed out by Schulz et al. (2003), θ^1 Ori C is one of many early-type stars in OB associations with hard X-ray spectra. The MCWS model may be fruitfully applied to τ Sco, and other young, early-type stars that show relatively narrow X-ray emission lines, hard X-ray spectra, and time variability.

REFERENCES

Anders, E., & Grevesse, N. 1989, Geochim. Cosmochim. Acta, 53, 197
Aufdenberg, J. P. 2001, PASP, 113, 119
Babel, J., & Montmerle, T. 1997a, A&A, 323, 121
———. 1997b, ApJ, 485, L29
Blumenthal, G. R., Drake, G. W. F., & Tucker, W. H. 1972, ApJ, 172, 205
Cassinelli, J. P., Miller, N. A., Waldron, W. L., MacFarlane, J. J., & Cohen, D. H. 2001, ApJ, 554, L55
Cohen, D. H., de Messières, G. E., MacFarlane, J. J., Miller, N. A., Cassinelli, J. P., Owocki, S. P., & Liedahl, D. A. 2003, ApJ, 586, 495
Cohen, D. H., Kramer, R. H., & Owocki, S. P. 2002, in High-Resolution X-Ray Spectroscopy with *XMM-Newton* and *Chandra*, ed. G. Branduardi-Raymont (London: Mullard Space Science Laboratory), http://www.mssl.ucl.ac.uk/~gbr/rgs_workshop/papers/dcohen_mssl.ps
Conti, P. S. 1972, ApJ, 174, L79
Dessart, L., & Owocki, S. P. 2003, A&A, 406, L1
———. 2005, A&A, 432, 281
Donati, J.-F., Babel, J., Harries, T. J., Howarth, I. D., Petit, P., & Semel, M. 2002, MNRAS, 333, 55
Drew, J. E. 1989, ApJS, 71, 267

Feldmeier, A. 1995, A&A, 299, 523
Feldmeier, A., Oskinova, L., & Hamann, W.-R. 2003, A&A, 403, 217
Feldmeier, A., Puls, J., & Pauldrach, A. W. A. 1997b, A&A, 322, 878
Gabriel, A. H., & Jordan, C. 1969, MNRAS, 145, 241
Gagné, M., Caillault, J., Stauffer, J. R., & Linsky, J. L. 1997, ApJ, 478, L87
Hillier, D. J., Kudritzki, R. P., Pauldrach, A. W., Baade, D., Cassinelli, J. P., Puls, J., & Schmitt, J. H. M. M. 1993, A&A, 276, 117
Howarth, I. D., & Prinja, R. K. 1989, ApJS, 69, 527
Ignace, R. 2001, ApJ, 549, L119
Ignace, R., & Gayley, K. G. 2002, ApJ, 568, 954
Kahn, S. M., Leutenegger, M. A., Cottam, J., Rauw, G., Vreux, J.-M., den Boggende, A. J. F., Mewe, R., & Güdel, M. 2001, A&A, 365, L312
Kramer, R. H., Cohen, D. H., & Owocki, S. P. 2003a, ApJ, 592, 532
Kramer, R. H., Tonnesen, S. K., Cohen, D. H., Owocki, S. P., ud-Doula, A., & MacFarlane, J. J. 2003b, Rev. Sci. Instrum., 74, 1966
Lucy, L. B., & Solomon, P. M. 1970, ApJ, 159, 879
MacDonald, J., & Bailey, M. E. 1981, MNRAS, 197, 995
MacFarlane, J. J., Cassinelli, J. P., Welsh, B. Y., Vedder, P. W., Vallerga, J. V., & Waldron, W. L. 1991, ApJ, 380, 564

MacFarlane, J. J., Golovkin, I., Woodruff, P., & Wang, P. 2003, APS Meeting Abst. 1181
MacGregor, K. B., Hartmann, L., & Raymond, J. C. 1979, ApJ, 231, 514
Miller, N. A., Cassinelli, J. P., Waldron, W. L., MacFarlane, J. J., & Cohen, D. H. 2002, ApJ, 577, 951
Morrison, R., & McCammon, D. 1983, ApJ, 270, 119
Owocki, S. P., Castor, J. I., & Rybicki, G. B. 1988, ApJ, 335, 914
Owocki, S. P., & Cohen, D. H. 2001, ApJ, 559, 1108
Owocki, S. P., & Puls, J. 1999, ApJ, 510, 355
Owocki, S. P., & Rybicki, G. B. 1984, ApJ, 284, 337
———. 1985, ApJ, 299, 265
Prinja, R. K., Barlow, M. J., & Howarth, I. D. 1990, ApJ, 361, 607
Raymond, J. C., Cox, D. P., & Smith, B. W. 1976, ApJ, 204, 290
Reiners, A., Stahl, O., Wolf, B., Kaufer, A., & Rivinius, T. 2000, A&A, 363, 585
Runacres, M. C., & Owocki, S. P. 2002, A&A, 381, 1015
Rybicki, G. B., & Lightman, A. P. 1979, Radiative Prosesses in Astrophysics (New York: Wiley)
Schertl, D., Balega, Y. Y., Preibisch, T., & Weigelt, G. 2003, A&A, 402, 267
Schulz, N. S., Canizares, C., Huenemoerder, D., & Lee, J. C. 2000, ApJ, 545, L135
Schulz, N. S., Canizares, C., Huenemoerder, D., & Tibbets, K. 2003, ApJ, 595, 365

Shore, S. N., & Brown, D. N. 1990, ApJ, 365, 665
Shore, S. N., Brown, D. N., Sonneborn, G., Landstreet, J. D., & Bohlender, D. A. 1990, ApJ, 348, 242
Smith, M. A., Cohen, D. H., Gu, M. F., Robinson, R. D., Evans, N. R., & Schran, P. G. 2004, ApJ, 600, 972
Smith, M. A., & Fullerton, A. W. 2005, PASP, 117, 13
Smith, M. A., & Groote, D. 2001, A&A, 372, 208
Smith, R. K., Brickhouse, N. S., Liedahl, D. A., & Raymond, J. C. 2001, ApJ, 556, L91
Stahl, O., Wolf, B., Gang, T., Gummersbach, C., Kaufer, A., Kovacs, J., Mandel, H., & Szeifert, T. 1993, A&A, 274, L29
Stahl, O., et al. 1996, A&A, 312, 539
ud-Doula, A., & Owocki, S. P. 2002, ApJ, 576, 413
Walborn, N. R. 1981, ApJ, 243, L37
Walborn, N. R., & Nichols, J. S. 1994, ApJ, 425, L29
Waldron, W. L., & Cassinelli, J. P. 2001, ApJ, 548, L45
Weigelt, G., Balega, Y., Preibisch, T., Schertl, D., Schöller, M., & Zinnecker, H. 1999, A&A, 347, L15
Yamauchi, S., & Koyama, K. 1993, ApJ, 405, 268
Yamauchi, S., Koyama, K., Sakano, M., & Okada, K. 1996, PASJ, 48, 719

ERRATUM: "*CHANDRA* HETGS MULTIPHASE SPECTROSCOPY OF THE YOUNG MAGNETIC O STAR θ^1 ORIONIS C" (ApJ, 628, 986 [2005])

Marc Gagné, Mary E. Oksala, David H. Cohen, Stephanie K. Tonnesen, Asif ud-Doula, Stanley P. Owocki, Richard H. D. Townsend, and Joseph J. MacFarlane

Figure 13 of our paper shows the dependence of the forbidden-to-intercombination line ratio on formation radius and electron density for two He-like ions, Mg xi and S xv, assuming a 45,000 K photosphere. In calculating the PRISMSPECT line ratios, we neglected to include the flux from the upper $^3P_2 \rightarrow {}^1S_0$ transition. For lower-Z ions such as Mg xi, the intercombination doublet is dominated by flux from the lower transition. But for higher-Z elements, this omission led us to underestimate the intercombination line strength from our model.

In addition, comparing the spectral type and luminosity of θ^1 Ori C with the recent calibrations of P. Massey et al. (ApJ, 627, 477 [2005]) and F. Martins et al. (A&A, 436, 1049 [2005]) suggests that θ^1 Ori C is an O5.5 V star with radius $R \approx 10.6\ R_\odot$ and effective temperature $T_{\rm eff} \approx 40,000$ K. This new calibration makes θ^1 Ori C larger and cooler than both the "hot" and "cool" models in Table 3 of our original paper.

In the revised Figure 13 below, we show the corrected PRISMSPECT line ratios for Mg xi, Si xiii, and S xv as a function of $u = R_\star/R$ for $T_{\rm eff} = 40,000$ K. Also shown are the predictions from the analytic parametrization of G. R. Blumenthal et al. (ApJ, 172, 205 [1972]). For Mg xi and Si xiii, we further show the predictions based on the R_0 values of D. Porquet et al. (A&A, 376, 1113 [2001]). The hatched regions in Figure 13 represent the 1 σ upper and lower bounds on f/i from the HETG data and $u = R_\star/R$ from the PRISMSPECT model. Although the three f/i ratios yield different bounds on the formation radius, there is a range of radii, $1.7 < R/R_\star < 2.1$, that is consistent with all three measured f/i ratios. Using G. R. Blumenthal et al. (ApJ, 172, 205 [1972]) (Fig. 13, *solid lines*), the range of radii is $1.6 < R/R_\star < 2.0$. The net effect of the corrected model and lower effective temperature is to place the X-ray–emitting plasma at a slightly larger radius than reported originally.

Figure 5c added here is a gray-scale image of emission measure per unit volume from the 375 ks snapshot of the MHD simulation shown in the upper and lower panels of Figure 5 of the original paper. Overlaid on the emission-measure map is a $T = 10^6$ K contour. The new Figure 5c shows that the X-rays in the magnetically channeled wind shock (MCWS) model are formed over a range of radii, with an effective emission radius $R \approx 2R_\star$, consistent with the revised f/i ratio calculations.

Thus, the only remaining discrepancy between the HETG data and the MCWS model is the overall X-ray variability, $1 - L_{\rm X}^{\rm min}/L_{\rm X}^{\rm max} \approx 0.33$. If the X-rays are produced, on average, at $R \approx 2R_\star$, then occultation of an X-ray torus by the photosphere would produce a $\sim$17% dip in visible X-ray luminosity at phase 0.5, only about half the observed drop. We suggest that the remaining absorption must occur in the dense gas in the magnetic equatorial plane. To test this idea, future absorption models will need to properly account for the ionization of the outflowing circumstellar plasma.
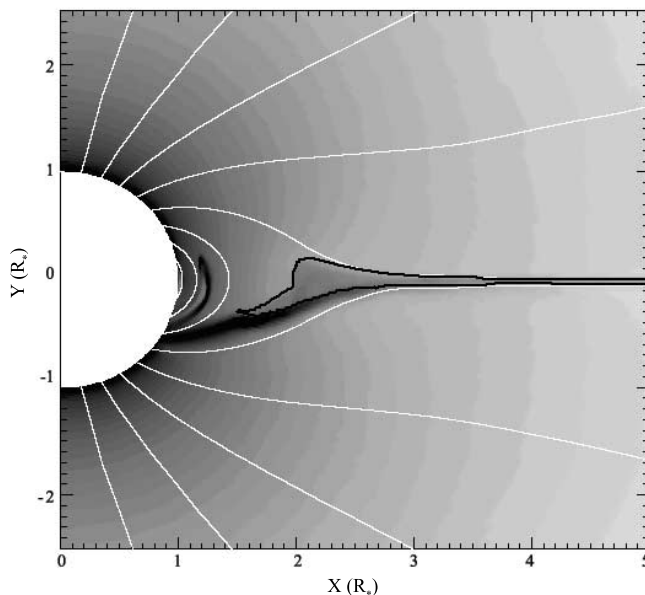
Fig. 5.—(*c, new panel*) Gray-scale snapshot of emission measure per unit volume from the 500 ks, slow-wind, two-dimensional MHD simulation of θ^1 Ori C. This snapshot was obtained at a typical simulation time $t = 375$ ks, when dense gas in the magnetic equatorial plane is falling back onto the photosphere. The dark $T = 10^6$ K contour suggests that, on average, the X-rays are produced at $R \approx 2R_\star$.
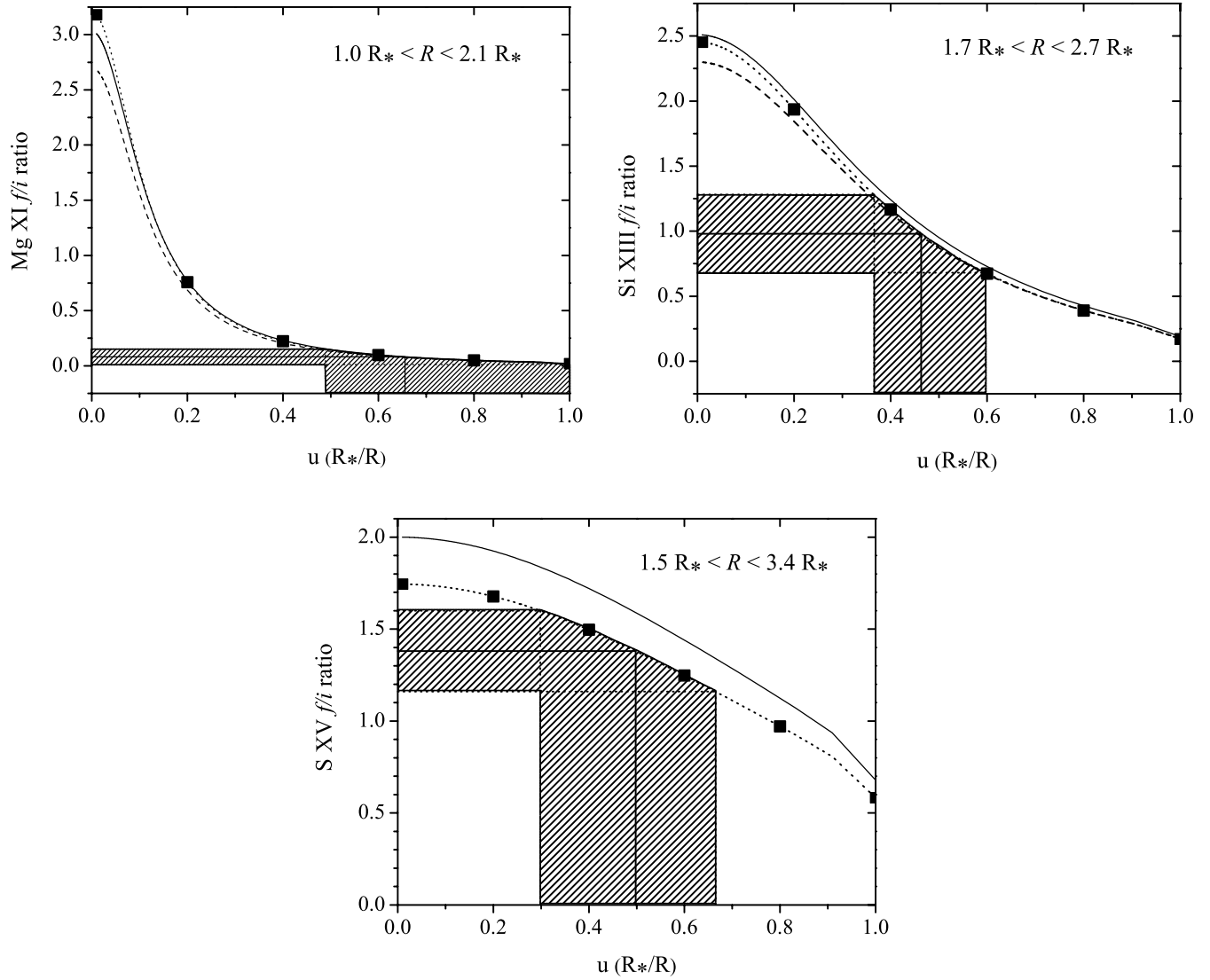
FIG. 13.—Forbidden-to-intercombination line f/i ratios vs. $u = R_{\star}/R$ for three He-like ions: Mg XI, Si XIII, and S XV, assuming a photospheric temperature $T_{\text{eff}} = 40,000$ K. The hatched regions represent the 1 σ upper and lower bounds on the observed f/i ratios and the corresponding bounds on $u = R_{\star}/R$ from the PRISMSPECT model (*dotted line and filled squares*), G. R. Blumenthal et al. (ApJ, 172, 205 [1972]; *solid line*), and D. Porquet et al. (A&A, 376, 1113 [2001]; *dashed line*).